Atmospheric bias teleconnections associated with systematic SST errors in the tropical Indian Ocean

Yuan-Bing Zhao[1], Nedjeljka Žagar[1], Frank Lunkeit[1], and Richard Blender[1]

[1]Meteorologisches Institut, Universität Hamburg, Hamburg, Germany

Correspondence: Yuan-Bing Zhao (yuan-bing.zhao@uni-hamburg.de)

Abstract. State-of-the-art climate models suffer from significant sea surface temperature (SST) biases in the tropical Indian Ocean (TIO), greatly damaging the climate prediction and projection. In this study, we investigate the multidecadal atmospheric bias teleconnections caused by the TIO SST bias and their impacts on the simulated atmospheric variability. A set of century long simulations forced with idealized SST perturbations, resembling various persistent TIO SST biases in coupled climate models, are conducted with an intermediate complexity atmospheric model. Bias analysis is performed using the normal-mode function decomposition which can differentiate between balanced and unbalanced flow regimes across spatial scales. The results show that the atmospheric circulation biases caused by the TIO SST bias have the Gill-Matsuno-type pattern in the tropics and Rossby wave-train distribution in the extratropics, similar to the steady state response to tropical heating. The teleconnection between the tropical and extratropical biases is set up by the Rossby wave-train emanating from the subtropics. Over 90% of the bias variance is contained in planetary scales (zonal wavenumber $k \leq 5$). These biases have great impacts on the simulated energy and interannual variance (IAV). The zonal-mean-flow energy and the extratropical (balanced) wave-flow energy responses are closely related to bias phase (i.e., the covariance between the bias and reference state). In contrast, the tropical (both unbalanced and balanced) wave-flow energy responses are primarily associated with bias amplitude. The response of the IAV is contingent upon the sign of the SST bias. A positive SST bias reduces the IAV, whereas a negative SST bias increases it, regardless of dynamical regimes. Geographically, strong IAV responses are observed in the tropical Indo-west Pacific region, Australia, south and northeast Asia, the Pacific-North America region and Europe, where the background IAVs are strong.

1 Introduction

The tropical Indian Ocean (TIO) plays an important role in climate variability (e.g. Schott et al., 2009; Beal et al., 2020; Hermes et al., 2019), and a realistic representation of the TIO sea surface temperature (SST) in the ocean-atmosphere coupled general circulation models (CGCMs) is crucial for the accurate prediction of both local and remote climate. However, state-of-the-art CGCMs exhibit large systematic errors (called biases) in the TIO SST (Li and Xie, 2012), which inevitably affect the accuracy of the atmospheric simulations (Joseph et al., 2012; Levine and Turner, 2012; Prodhomme et al., 2014).

The TIO SST biases greatly vary in amplitude and sign among the models involved in the Coupled Model Inter-comparison Project (CMIP). About half of the CMIP5 models show positive SST biases over the western TIO during boreal summer

(Fathrio et al., 2017; Lyon, 2020). For example, the SINTEX-F2 model has a warm SST bias in the tropics, and especially over the western TIO region (Joseph et al., 2012) and the bias is nearly constant throughout the annual cycle (Prodhomme et al., 2014). Other half of the CMIP5 models show negative SST biases over the entire TIO region throughout the year (Wang et al., 2014; Fathrio et al., 2017). For example, the HadCM3 model has a large-magnitude, cold SST bias in winter and spring in the
30 Arabian Sea (Turner et al., 2005; Levine and Turner, 2012). Similar cold bias is present in most CMIP6 models (Wang et al., 2022). On the other hand, a significant warm SST bias in the TIO region was also recently reported in the CMIP6 models, which was not evident in the CMIP5 models (Zhang et al., 2023). Furthermore, the realistic representation of the Indian Ocean Dipole (IOD) in climate models remains a challenge since it is overly strong in all generations of CMIP models (Cai and Cowan, 2013; Weller and Cai, 2013), visible as IOD-like SST biases in the majority of the CMIP5 models (Li et al., 2015).
35 Moreover, the IOD-like SST biases are even stronger in the CMIP6 models than in the CMIP5 models (McKenna et al., 2020).

The long-standing TIO SST biases greatly impact the skill of climate prediction. Locally, the TIO SST biases modify the local meridional SST gradient and affect the Indian Summer Monsoon, leading to biases in precipitation (Joseph et al., 2012; Levine and Turner, 2012; Bollasina and Ming, 2013; Annamalai et al., 2017; Prodhomme et al., 2014). Besides, an SST increase
40 from 26.5 to 28.0 °C has been shown by both observations and simulations to drastically change the convective response from shallow to deep convection (e.g., Gadgil et al., 1984; Roxy et al., 2014).

The impact of TIO SST biases on the simulated atmospheric variability in remote regions is more difficult to understand, and studies on it are rare. Annamalai et al. (2007) performed idealized numerical experiments and showed that the diabatic heating associated with the TIO seasonally varying SST anomalies can generate Rossby wave packets which set up the tele-
45 connection between the TIO and the Pacific-North American (PNA) region and impact considerably the Northern Hemisphere (NH) extratropical circulation. This implies that the TIO SST biases could also cause atmospheric circulation biases in extratropics. Indeed, remote bias coupling has been reported before. Wang et al. (2014) studied the CMIP5 model biases from a global perspective. They found that biases in local regions can be linked with others in far away regions. Recently, Bai et al. (2023) showed that the tropical west Pacific warm bias in the Unified Forecast System (UFS) coupled model can influence the
50 simulated north American precipitation remotely through the wave-activity flux.

The present study extends existing research of the effects of systematic errors in the TIO SST on the global atmospheric variability by using a perfect atmosphere model framework. Within this framework, we carry out centennial control simulations forced with the observed SST and compare them with simulations that have systematic errors in the TIO SST. We hypothesize that TIO SST biases induce biases in the simulated atmospheric circulation not only in the tropics but also in the extratrop-
55 ics through tropics-extratropical coupling and that TIO SST biases affect the interannual variability across scales. Specific questions addressed are the following:

– What is the spatial structure of biases in simulated circulation in the tropics and extratropics? What scales are most affected?

– What are the dynamical mechanisms that connect the TIO SST bias to biases in simulated circulation?

60   – How do spatial and temporal variability change in response to the TIO SST biases?

The global perspective of circulation biases in response to localised SST biases has hardly been addressed. We attempt at providing this perspective for the case of Indian Ocean SST using an intermediate complexity climate model and a novel method for the flow decomposition. The application of a reduced complexity climate model Planet Simulator (Fraedrich et al., 2005) allows us to carry out a large number of centennial length simulations with prescribed SST biases.

65   The analysis method includes the scale and regime decomposition using the modal decomposition as in Žagar et al. (2020) and Castanheira and Marques (2022). Žagar et al. (2020) introduced the global perspective for studying effects of biases on simulated variability in climate models. They quantified changes in the interannual variability at planetary scales and in the mean flow due to errors in their slab-ocean model coupled to the atmosphere model. Even the atmospheric small-scale variance in their perfect atmosphere model had sufficient amplitude, which was associated with biases in the simulated annual energy

70 cycle. Castanheira and Marques (2022) found that the presence of cold SST bias in North Pacific in CMIP6 models may compensate for the biases in the North Pacific barotropic atmospheric variability through influence on the excitation of the most unstable barotropic mode of the atmospheric circulation.

The rest of this paper is organized as follows. In Section 2, we describe the Planet Simulator and the experiment design, followed by the description of method for the quantification of circulation biases. The method follows Žagar et al. (2020) but

75 it is here applied in its complete formulation and for the quasi-geostrophic (or balanced) midlatitude dynamical regime and largely unbalanced tropical circulation. The results are presented in Section 3, including the total circulation biases, the regime-dependent biases, the underlying physics of remote bias coupling and its impacts on the simulated spatio-temporal variability. The study is summarized in Section 4.

2   Methodology

80 We first present the design of numerical experiments with the Planet Simulator model (PLASIM; Fraedrich et al., 2005; Fraedrich and Lunkeit, 2008). This is followed by the description of the normal-mode function (NMF) decomposition and definition of quantities analysed in spectral and physical space.

2.1   Climate model and experiment design

2.1.1   The model

85 PLASIM models the atmospheric dynamics using primitive equations in σ-coordinate, $\sigma = p/p_s$, where p and p_s denote the pressure and the surface pressure, respectively. The prognostic variables are vorticity, divergence, temperature, specific humidity and the logarithm of the surface pressure. The hydrostatic primitive equations are solved using the spectral transformation methods (Eliassen et al., 1970; Orszag, 1970). Unresolved processes are parameterized, which include the long-wave (Sasamori, 1968) and short-wave (Lacis and Hansen, 1974) radiation, interactive clouds (Stephens, 1978, 1984; Slingo and

90 Slingo, 1991), moist (Kuo, 1965, 1974) and dry convection, large-scale precipitation, the horizontal and vertical diffusion

(Louis, 1979; Louis et al., 1982; Laursen and Eliasen, 1989; Roeckner et al., 1992), and boundary-layer parameterization including latent and sensible heat fluxes (Louis, 1979). For more information on the model, the reader is referred to Fraedrich et al. (2005).

In this study, we run PLASIM with prescribed SST and sea ice content. We adopt a T31 horizontal resolution (approximately 3.75°×3.75° on the corresponding 96×48 Gaussian grid) and ten σ levels: 0.038, 0.119, 0.211, 0.317, 0.437, 0.567, 0.699, 0.823, 0.924, 0.983.

2.1.2 Atmosphere-ocean coupling in PLASIM

With the SST fixed, the atmosphere and ocean surface communicate by exchanging the heat and moisture. The bulk aerodynamic formulas for the surface fluxes are

$$F_T = \rho c_p C_H |\mathbf{V}| (\text{SST} - T_{\text{air}}), \tag{1}$$

$$F_q = \rho C_H C_W |\mathbf{V}| (q_{\text{sea}} - q_{\text{air}}), \tag{2}$$

where F_T and F_q are the sensible heat flux and the moisture flux, respectively. The constant parameters in the formulas are defined as follows: ρ is air density, c_p is the specific heat at constant pressure, C_H is the transfer coefficient for heat, and C_W is the wetness factor accounting for different evaporation efficiencies due to surface characteristics. The fluxes depend on the values of prognostic variables at the lowermost model level: $|\mathbf{V}|$, T_{air} and q_{air}, i.e. the horizontal wind speed, air temperature and specific humidity, and the specific humidity at the sea surface, q_{sea} which is assumed to be saturated and has a temperature equal to the SST. Given the SST, the saturation water vapor pressure e_{sat} is computed using the Claussius-Clapeyron equation for SST in degrees Celsius as

$$e_{\text{sat}} = 610.78 \exp\left(\frac{17.27\text{SST}}{\text{SST} + 237.30}\right). \tag{3}$$

Then q_{sea} is produced making use of instantaneous value of surface pressure p_s as

$$q_{\text{sea}} = \frac{\epsilon e_{\text{sat}}}{p_s - (1-\epsilon)e_{\text{sat}}}, \tag{4}$$

where ϵ is the ratio of the gas constant for dry air R_d and water vapor R_v ($\epsilon = R_d/R_v$). A positive F_T means heat is flowing from the surface to the atmosphere. A positive F_q means water is evaporating from the surface with latent heat. Both terms exhibit seasonal variations. The globally averaged climatological annual mean F_T in PLASIM forced with SST from the ERA-20C reanalyses (Poli et al., 2016) is estimated to be 20.5 W m^{-2} and the seasonal variation of F_T spans from -14.2% to 15.4% of the annual mean. The globally averaged climatological annual mean F_q is measured at 2.8 kg m^{-2} day^{-1}, corresponding to a latent heat flux of 81.2 W m^{-2}, and the seasonal variation of F_q ranges from -4.4% to 6.6% of the annual mean.

The fluxes at the sea surface are closely coupled with the cumulus convection. In PLASIM, convection is parameterized by a Kuo-type scheme (Kuo, 1974), where an important quantity involved is the net precipitation rate which is proportional to the

net amount of the horizontal moisture flux convergence (MFC) plus the moisture supply by surface evaporation (i.e., F_q)

$$P_r = -\frac{p_s}{g} \int_0^1 \nabla \cdot (q\mathbf{V}) \mathrm{d}\sigma + F_q.$$ (5)

The above equations show that a systematic local increase in SST will lead to locally more upward sensible heat and moisture flux, which will lower the near-surface moist static stability. Stronger convection and more precipitation (P_r) will occur leading to greater latent heat release and stronger effects on atmospheric circulation.

2.1.3 Experimental design

A set of century long simulations are carried out using a perfect-model framework. In this framework, the only difference between the reference (or control) and sensitivity simulations is the SST perturbation in the Indian Ocean which represents the climate model SST bias. Differences between the simulations therefore originate from differences in the TIO SST.

The reference simulation is forced with the time-varying monthly mean SST including interannual variations from the ERA-20C reanalyses (Poli et al., 2016). Four sensitivity experiments apply the same SST with addition of time-constant perturbations in the TIO region that mimic TIO SST biases found in the CGCMs (e.g., Li et al., 2015; Fathrio et al., 2017; Lyon, 2020). In other words, the steady SST perturbations in this study represent the SST biases (or systematic errors).

Table 1. Configurations of the SST perturbations.

Experiments	T_0 (in K)	λ_0	φ_0	σ_x	σ_y
EXP_POS	1.5	70° E	0°	20	15
EXP_NEG	-1.5	70° E	0°	20	15
EXP_10N	1.5	70° E	10° N	20	15
EXP_IOD	1.5/-1.5	55° E/105° E	0°	15	15

The spatial structure of the SST perturbation is given by

$$\Delta\mathrm{SST}(\lambda, \varphi) = \begin{cases} T_0 \exp\left[-\frac{(\lambda - \lambda_0)^2}{\sigma_x{}^2} - \frac{(\varphi - \varphi_0)^2}{\sigma_y{}^2}\right], & |\Delta\mathrm{SST}| > 0.05; \\ 0, & \text{otherwise}; \end{cases}$$ (6)

where T_0 determines the maximal magnitude, (λ_0, ϕ_0) specifies the center location, and σ_x and σ_y define the perturbation extent. The parameters of the four perturbations are listed in Table 1.

The distributions of SST perturbations are shown in Fig. 1. In one experiment, a monopolar SST perturbation with a maximum of +1.5 K is centered at the equator and covers the entire TIO region (Fig. 1a). Another one applies the same SST perturbation but with the opposite sign (i.e., negative SST error; Fig. 1b). For convenience, we refer to this experiment as EXP_NEG and the previous one as EXP_POS. The third experiment is the same as EXP_POS but the SST perturbation is shifted 10° northward, and the experiment is labeled as EXP_10N (Fig. 1c). The forth simulation applies a dipolar SST perturbation which mimics the IOD-type bias (e.g., Cai and Cowan, 2013; McKenna et al., 2020) and is referred to as EXP_IOD
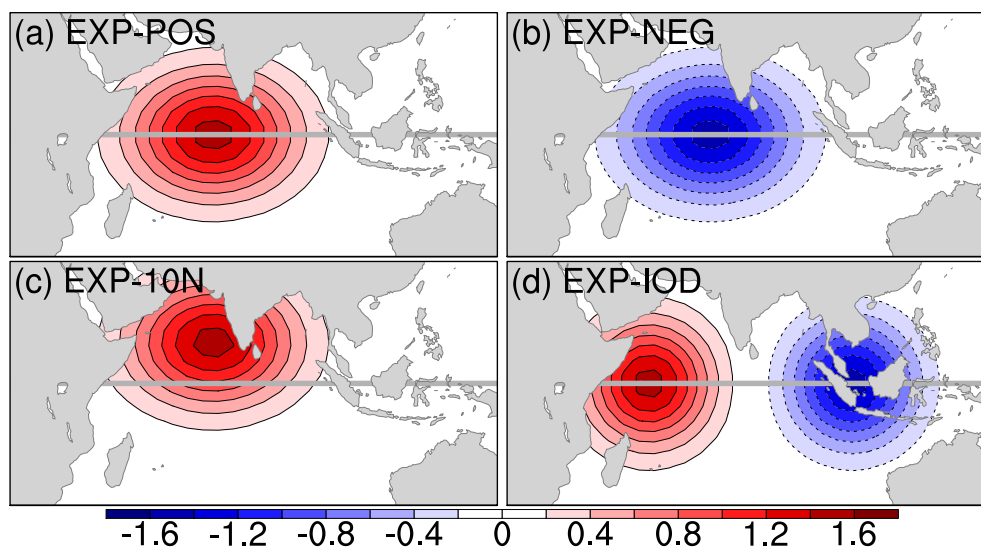
Figure 1. SST perturbations (in K) used in the sensitivity experiments. The gray line marks the equator.

(Fig. 1d). In the equatorial Indian Ocean, the SST peaks in April at about 29.5 °C and minimizes in December, around 28 °C. In other words, the seasonal variation is about 1.5 °C, equal to the amplitude of the SST perturbation used in this study.

145   For each experiment, the model starts on 1 January 1901 and the simulation ends on 31 December 2010. The initial condition comes from a 40-year spin-up run (i.e., an equilibrium state) forced by the climatological monthly mean ERA-20C SST (without interannual variation). In the reference simulation, the heat fluxes at the Earth's surface and the top of the atmosphere are found to be balanced (i.e., zero total heat flux) throughout the integration and the total atmospheric energy (kinetic energy plus potential energy) is conserved, even during the initialization. When a strong SST bias is applied, it will lead to the

150   breakdown in the model's surface-top heat flux balance during the first several months of the integration (not shown), which results in a net energy input (output) into (from) the atmosphere. After this short period, the surface-top heat flux balance recovers without further net energy input (output) into (from) the atmosphere, and the atmospheric total energy will remain at the level it attains. In this study, the SST bias applied is however too weak to affect the overall heat flux balance, and the total atmospheric energy is conserved over time. But note that the weak SST bias can result in notable modifications to the available

155   potential energy (and the kinetic energy), which are the primary focus of this study.

While the atmospheric circulation bias can be established in the first decade, the atmospheric variability takes several decades to become equilibrium. We therefore discard the first 30 integration years and use the last 80 years (1931-2010) in the analysis.

2.2 Decomposition of circulation biases

The outputs of numerical simulations are decomposed in terms of the Hough harmonics which provide scale and regime

160   information. Here we summarise the concept and refer the reader to Žagar et al. (2015) which describes details of the applied

MODES software. Once the global circulation is decomposed, statistics of biases and interannual variance (IAV) can be carried out in spectral (or modal) space as outlined below.

2.2.1 Modal decomposition

The scale and regime decomposition of the 3D global circulation relies on the representation of the global baroclinic atmosphere
165 in terms of M global shallow-water systems, each characterized by own fluid depth for the horizontal motions that is known as the equivalent depth. The non-dimensional oscillations of the horizontal wind and geopotential height fields in various systems are coupled through equivalent depth, denoted as D, with the vertical structure equation. Given a vertical mode m $(m = 1, ..., M)$, the horizontal motions are represented by a series of Hough harmonics which are the product of the Hough vector functions in the meridional direction and waves in the longitudinal direction. The complex Hough expansion coefficient
170 $\chi_n^k(m)$, which represents the two wind components (u, v) and the geopotential height h, is obtained as

$$\chi_n^k(m) = \frac{1}{2\pi} \int\limits_{0}^{2\pi} \int\limits_{-1}^{1} \left(\mathbf{S}_m^{-1} \sum_{j=1}^{J} (u, v, h)^T G_m(j) \right) \cdot [\mathbf{H}_n^k(m)]^* \, d\mu \, d\lambda, \qquad (7)$$

where the asterisk $(*)$ denotes the complex conjugate. Equation (7) describes a 2-step procedure which consists of the vertical projection (within the parenthesis) followed by the horizontal step. The vertical structure functions $G_m(j)$ are orthogonal and solved by using the finite difference method for the atmosphere discretized by J σ-levels. The basis functions for the
175 horizontal projection are the Hough harmonics, denoted by $\mathbf{H}_n^k(\varphi; m)$. For every given vertical mode, the Hough harmonics are characterized by the two indices for the zonal wavenumber k and meridional mode n. The scaling matrix $\mathbf{S}_m$ is a 3×3 diagonal matrix which makes the input data vector after the vertical projection dimensionless. Parameters λ and φ stand for the geographical longitude and latitude, respectively, whereas $\mu = sin(\varphi)$.

A discrete solution of Eq. (7) is obtained by replacing the integration by a finite series of the Hough harmonic functions
180 including the zonally-averaged state, K zonal waves and R meridional modes. The maximal number of meridional modes R combines N_R balanced modes, denoted as BAL, N_E eastward-propagating inertio-gravity modes, denoted as EIG, and N_W westward-propagating inertio-gravity modes which are denoted as WIG; $R = N_R + N_E + N_W$. The Kelvin wave is $n = 0$ EIG mode and the mixed Rossby-gravity wave is $n = 0$ Rossby mode.

In the projection of PLASIM simulations, we use a truncation similar to the model, that is $K = 30$, $M = 10$ and $N_R = $
185 $N_E = N_W = 30$ modes, meaning 30 modes for each of the wave species. This also means that our decomposition is complete, and the statistics, which is defined next, accounts for the complete variance in the system. In particular, both PLASIM and MODES are defined in the σ system. The projection is carried out on monthly-mean data.

2.2.2 Statistics in modal space

The second moments of the statistics are evaluated in terms of Hough coefficient $\chi_\nu(t)$, where a single modal index $\nu = $
190 (k, n, m). The total (kinetic plus available potential) energy contained in mode ν per unit area at time step t can be defined as

(Žagar et al., 2020)

$$I_\nu(t) = \frac{1}{2}gD_m\left|\chi_\nu(t)\right|^2,\tag{8}$$

with D_m the equivalent height of vertical mode m. I_ν is used to represent the spatial variance as in literature (e.g. Žagar et al., 2020). Then, the energy of the time-mean state (i.e., climatological energy) is

$$E_\nu = I(\overline{\chi_\nu}) = \frac{1}{2}gD_m\left|\overline{\chi_\nu}\right|^2\tag{9}$$

where

$$\overline{\chi_\nu} = \frac{1}{N}\sum_{t=1}^{N}\chi_\nu(t).\tag{10}$$

The temporal variance can be defined as

$$V_\nu = \frac{1}{N}\sum_{t=1}^{N}gD_m\left|\chi_\nu(t) - \overline{\chi_\nu}\right|^2\tag{11}$$

The global integration of V_ν is equivalent to the integral of the temporal variance in physical space

$$\sum_k\sum_n\sum_m V_\nu = \sum_i\sum_j w(\lambda_i,\varphi_j)\sum_{m=1}^{M}\left[S_m^u + S_m^v + S_m^h\right].\tag{12}$$

with $\tilde{u}_m$, $\tilde{v}_m$ and $\tilde{h}_m$ denoting the non-dimensionalized horizontal fields after the vertical projection. Here, $w(\lambda_i,\varphi_j)$ denotes the Gaussian weight, and

$$S_m^u = gD_m Var(\tilde{u}_m), \quad S_m^v = gD_m Var(\tilde{v}_m), \quad S_m^h = gD_m Var(\tilde{h}_m),\tag{13}$$

where $Var(x) = \frac{1}{N}\sum_{t=1}^{N}|x(t) - \overline{x}|^2$ denotes the temporal variance of any scalar variable x at location (λ_i, φ_j).

Assuming ergodicity, the difference between the time-mean energy and the climatological energy is equal to half the temporal variance (Žagar et al., 2020)

$$\overline{I_\nu} - E_\nu = \frac{1}{2}V_\nu.\tag{14}$$

Defining the time-mean energy of mode ν simulated by a GCM is $\overline{I_\nu^c}$ and that of the verifying data is $\overline{I_\nu^a}$, we obtain

$$\overline{I_\nu^c} - \overline{I_\nu^a} = \left[E_\nu^c - E_\nu^a\right] + \frac{1}{2}\left[V_\nu^c - V_\nu^a\right],\tag{15}$$

or in the form

$$\Delta\overline{I_\nu} = \Delta E_\nu + \frac{1}{2}\Delta V_\nu.\tag{16}$$

Here, superscripts c and a denote the GCM simulation and the verifying data (say analysis), respectively. It tells that changes in the time-mean energy is attributed to both changes in the climatological energy ΔE_ν and temporal variance ΔV_ν. Furthermore, ΔE_ν can be decomposed into two parts

$$\Delta E_\nu = B_\nu + P_\nu, \tag{17}$$

where B_ν is the bias variance (energy)

$$B_\nu = \frac{1}{2} g D_m \left| \overline{\Delta \chi_\nu} \right|^2, \tag{18}$$

with

$$\overline{\Delta \chi_\nu} = \frac{1}{N} \sum_{t=1}^{N} \left[\chi_\nu^c(t) - \chi_\nu^a(t) \right] \tag{19}$$

denoting the circulation bias in mode ν. The bias covariance P_ν is the covariance between the bias $\overline{\Delta \chi_\nu}$ and the time-averaged reference state $\overline{\chi_\nu^a}$:

$$P_\nu = \frac{1}{2} g D_m \left(\overline{\Delta \chi_\nu} \, \overline{\chi_\nu^a}^* + \overline{\Delta \chi_\nu}^* \, \overline{\chi_\nu^a} \right). \tag{20}$$

The two components of the bias represent the amplitude (B_ν) and phase (P_ν) of the bias. To see this, let $\overline{\chi_\nu^a} = \left| \overline{\chi_\nu^a} \right| e^{i\theta_A}$ and $\overline{\Delta \chi_\nu} = \left| \overline{\Delta \chi_\nu} \right| e^{i\theta_B}$, Eq. (20) becomes

$$P_\nu = g D_m \left| \overline{\chi_\nu^a} \right| \left| \overline{\Delta \chi_\nu} \right| \cos(\Delta\theta), \tag{21}$$

where $\Delta\theta = \theta_B - \theta_A$, denoting the phase difference between bias and reference state. If $|\Delta\theta| < \pi/2$, $P > 0$; otherwise, $P \leq 0$. Obviously, B_ν and P_ν are bias-related. Particularly, if the model is perfect (i.e., $\overline{\Delta \chi_\nu} = 0$), both terms vanish.
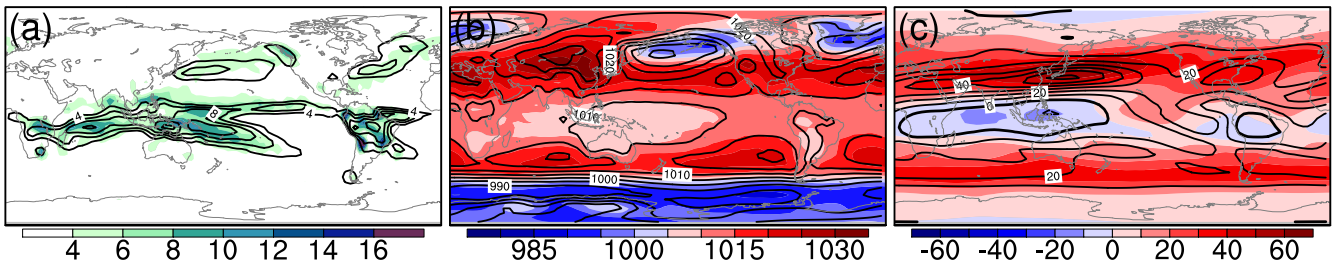
Figure 2. Long-term (1931-2010) mean DJF fields of the reference simulations (colors) overlaid with the ERA-20C reanalyses (contours): (a) total precipitation (mm day^{-1}), (b) mean sea level pressure (hPa) and (c) 250 hPa zonal wind (m s^{-1}).

3 Results

In this study, we aim at understanding the general principle behind the bias teleconnection rather than its seasonal variation. Indeed, the circulation bias in the tropics has the same pattern throughout the year only with varying magnitude, and the

extratropical biases are primarily observed in the Northern Hemisphere during boreal winter and in the Southern Hemisphere during boreal summer, albeit with much weaker intensity. We therefore narrow our focus exclusively to the boreal wintertime (December-January-February; DJF). In the following, we first validate the reference simulation before discussing the bias and
235 variability in sensitivity simulations.

3.1 Reference simulation

Figure 2 displays the DJF mean fields of the mean reference simulations and the ERA-20C fields. Overall, PLASIM is able to simulate the precipitation and the general circulation with correct patterns and magnitudes. For instance, the strong precipitation centers in the tropics are well simulated, which indicate the Inter-Tropical Convergence Zone (ITCZ) and the South Pacific
240 Convergence Zone (SPCZ) (Fig. 2a). In midlatitudes, strong precipitation is seen in the north Pacific and north Atlantic, where the atmospheric storm tracks are located. As for the circulation, the high-low pressure systems at the sea level (Fig. 2b) and zonal wind in the upper troposphere (Fig. 2c) are also well reproduced. But, there are also some discrepancies between the PLASIM simulation and the reanalysis. Particularly, the precipitation centers in the Bay of Bengal and the South China Sea are not well simulated (Fig. 2a). Besides, the precipitation in midlatitudes is generally underestimated and the precipitation center
245 over the north Pacific shifts northward compared with the reanalysis, which should be attributed to the northward shift of the Aleutian low (Fig. 2b) and the jet stream (Fig. 2c) over the north Pacific in the simulation. Nevertheless, these discrepancies are not unexpected given that PLASIM is a model of intermediate complexity.

In what follows, we validate sensitivity simulations against the reference simulation and according to Eq. (19) call their time averaged difference "bias".
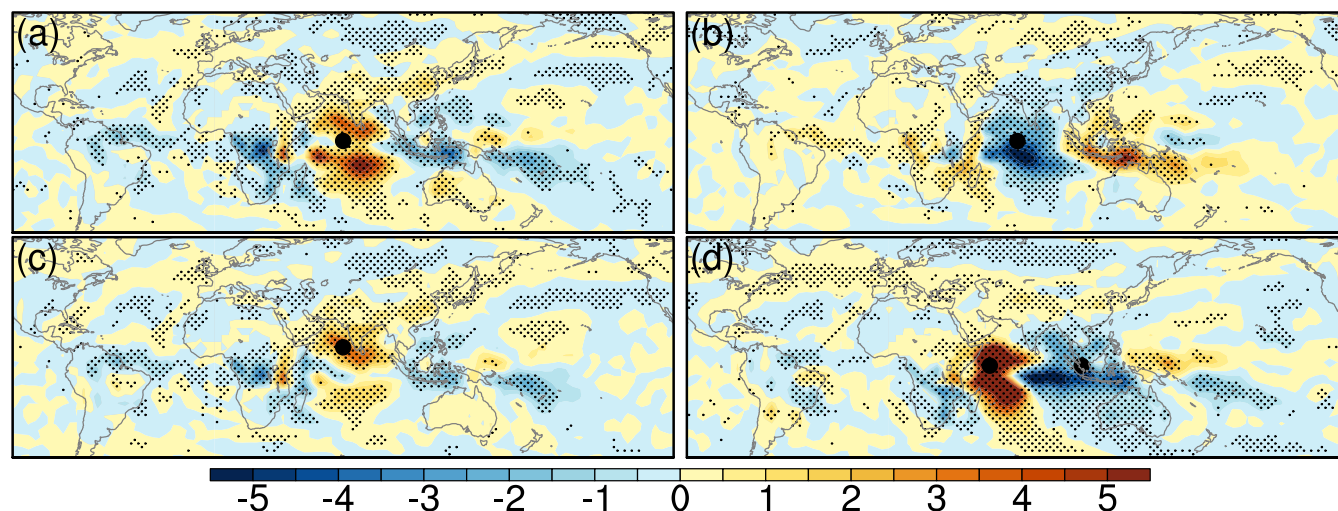
Figure 3. Distribution of the DJF precipitation biases (in mm day^{-1}): (a) EXP_POS, (b) EXP_NEG, (c) EXP_10N and (d) EXP_IOD. Dotted area shows the region of precipitation bias statistically significant at 0.05 level using the Student's t-test. The large black dot in each panel marks the location of the SST bias center (the same below).

3.2 Precipitation biases

Figure 3 shows the distribution of the DJF total precipitation biases, which is computed as the time-averaged difference between
the sensitivity and the reference simulations over the last 80 integration years (1931-2010). The strongest biases are confined
in the tropics. One prominent common feature among the four experiments is the wet (dry) bias in the area where positive
(negative) SST biases are applied. As explained in Section 2.1.2, this is attributed to the response of the local air-sea interaction
to the SST bias. The warm SST bias results in locally more upward sensible and moisture fluxes at the surface, lowering the
near-surface static stability, enhancing the low-level moisture convergence (Lindzen and Nigam, 1987; Back and Bretherton,
2009), and therefore bringing more deep convection and precipitation. The cold SST bias leads to opposite results, namely dry
bias in the TIO region (Fig. 3b).

Apart from the local response, significant biases are also seen in remote areas. Looking at EXP_POS (Fig. 3a), strong dry
biases are found roughly along the equator to the west and east of the TIO region. In particular, rain band associated with the
SPCZ is significantly reduced. Significant precipitation biases are also visible in the extratropics (e.g., East and North Asia and
north Pacific), but their magnitudes are small. These nonlocal precipitation biases are associated with the circulation biases
caused by the SST biases. We will come back to this later.

3.3 Tropical and extratropical circulation biases

In this section, we discuss biases in circulation decomposed in balanced (Rossby modes) and unbalanced (IG modes including
the tropical Kelvin and mixed Rossby-gravity modes) components. But first we present the total circulation bias, that is the
sum of the Rossby and IG components.

3.3.1 Total circulation biases

Biases in the horizontal circulation in boreal winter are shown in Fig. 4. In all sensitivity experiments, strong biases are mainly
observed in the tropics and the Northern Hemisphere. In the experiment with positive (negative) SST biases, anomalous winds
associated with negative (positive) geopotential height biases converge (diverge) at lower levels in the TIO area, whereas at
upper levels the winds diverge (converge); this indicates the Walker circulation bias on the zonal section which is closely
associated with the strong precipitation biases in the tropics (Fig. 3). In the extratropics, the bias centers at lower and upper
levels are generally in phase, indicating barotropic structure. These centers are organized as stationary Rossby wave-trains
linking the subtropics and mid-to-high latitudes, having some similarities to the simulation by Annamalai et al. (2007). They
should account for the extratropical precipitation biases (Fig. 3). In comparison, EXP_POS (Figs. 4a and 4b) and EXP_NEG
(Figs. 4c and 4d) exhibit similar circulation bias patterns but with opposite signs. Despite the northward shift of SST bias in
EXP_10N, its circulation biases (Figs. 4e and 4f) resemble those in EXP_POS (Figs. 4a and 4b). The strongest extratropical
bias centers are mainly observed over Pacific-North America (PNA) region in all experiments except EXP_IOD where they are
seen over North America, North Atlantic, Europe and northeast Asia (Figs. 4g and 4h).
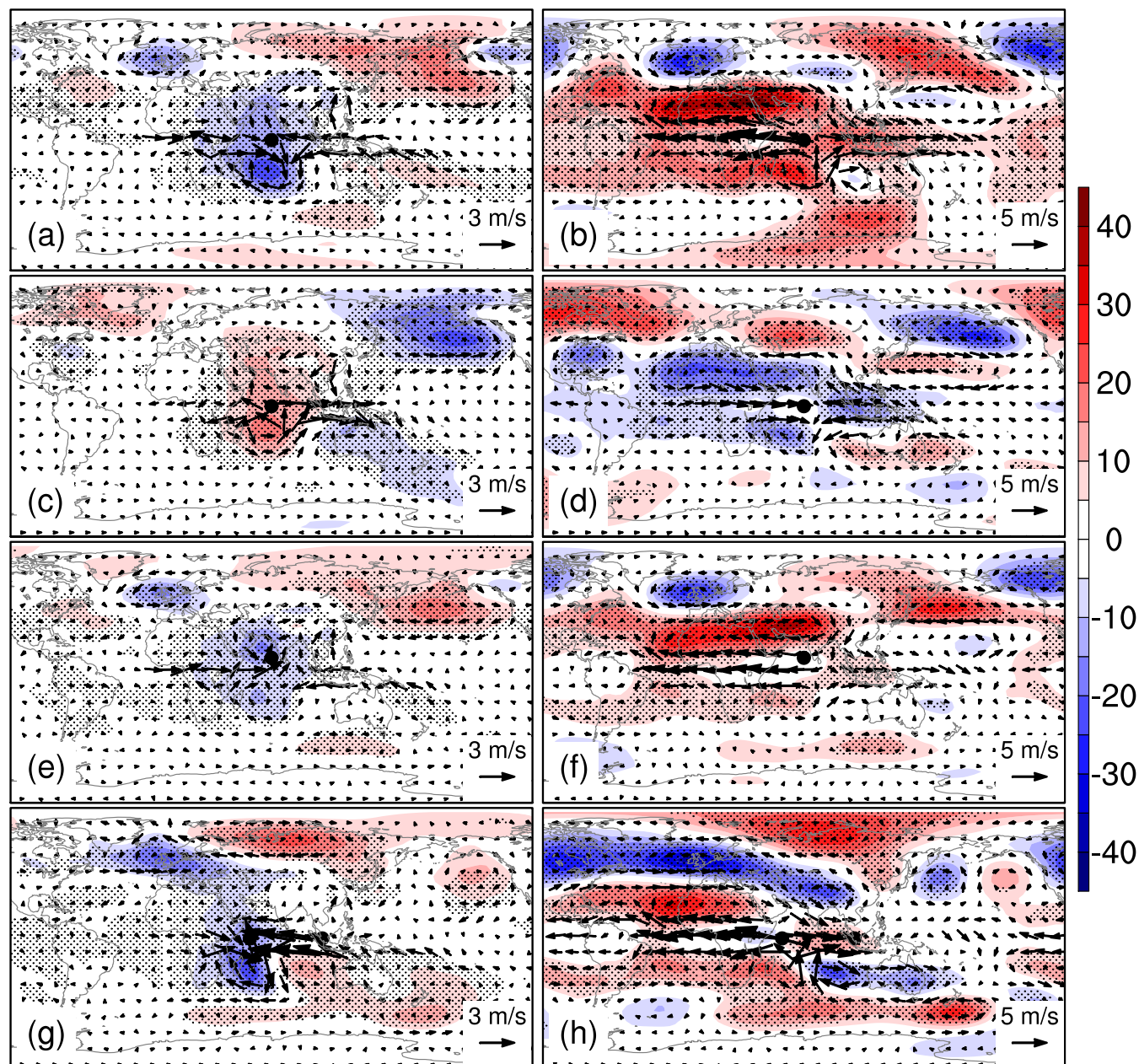
Figure 4. Total circulation biases in (a,b) EXP_POS, (c,d) EXP_NEG, (e,f) EXP_10N and (g,h) EXP_IOD at (left) $\sigma = 0.924$ and (right) $\sigma = 0.211$. Vectors stand for winds (in m s^{-1}) and colors for the geopotential height (in gpm). Dotted area shows the region of geopotential height biases statistically significant at 0.05 level using the Student's t-test.

In short, SST biases in the TIO region cause anomalous deep convection and thus anomalous diabatic heating, which ultimately leads to circulation biases worldwide. Nevertheless, the circulation biases are yet to fully understand since the balanced and unbalanced components are mixed together, especially in the tropics. In the following, we decompose the total circulation biases into the balanced and unbalanced regimes using the NMF decomposition for further discussions.
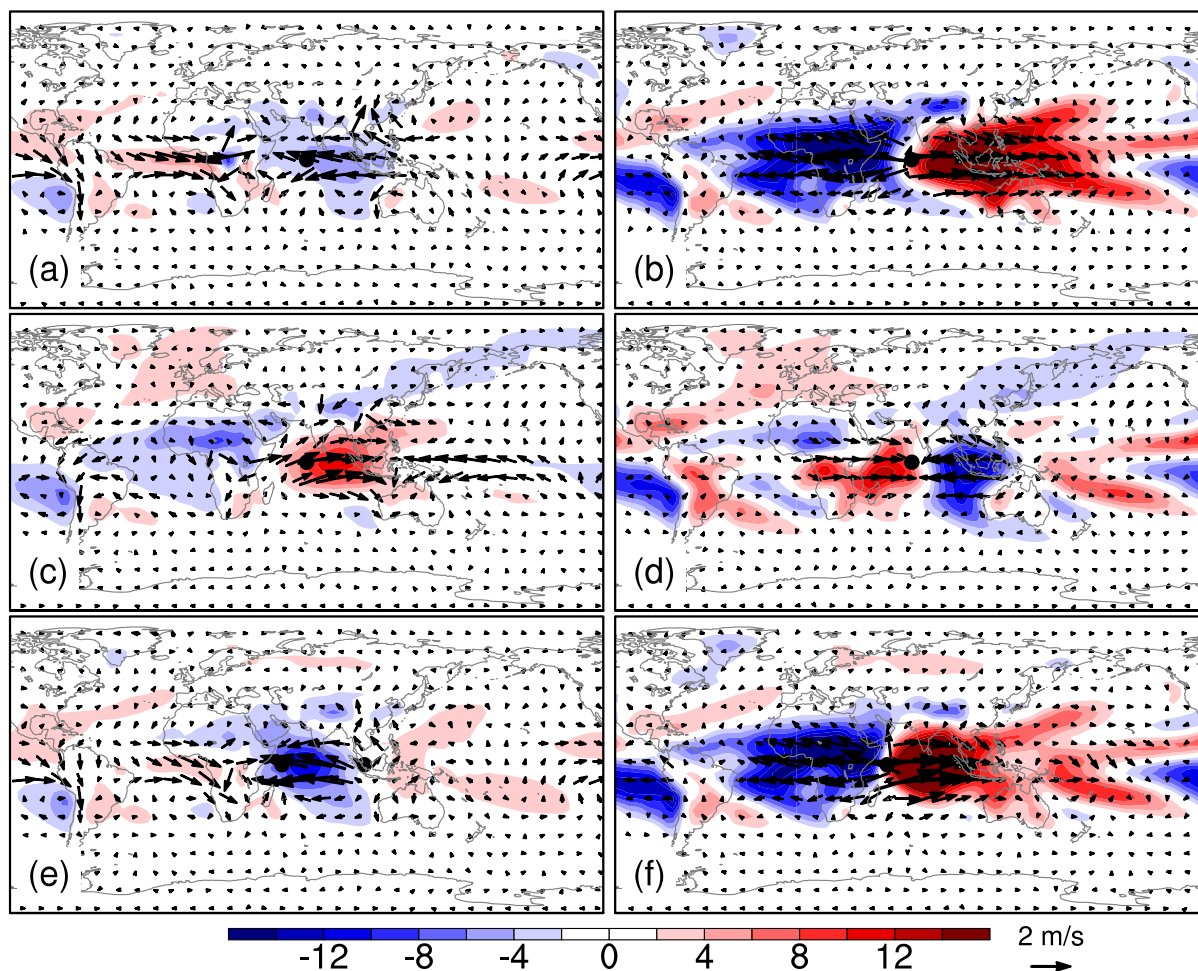
Figure 5. The unbalanced wave circulation biases in (a,b) EXP_POS, (c,d) EXP_NEG and (e,f) EXP_IOD at (left) $\sigma = 0.924$ and (right) $\sigma = 0.211$. Vectors stand for winds (in m s^{-1}) and colors for the geopotential height (in gpm). The zonal-mean (k=0) mode has been excluded.

3.3.2 Decomposition of biases in balanced and unbalanced components

285

We first look at the unbalanced circulation biases which are displayed in Fig. 5. They are reconstructed with the Hough coefficients of all unbalanced modes except the zonal-mean ($k = 0$) mode since we are more interested in the wave circulation.

The EXP_10N is not shown since it has quite similar results to EXP_POS (see Fig. 4). One common feature among these experiments is that the unbalanced biases are mainly confined in lower latitudes. They have the characteristics of the baroclinic

290 Kelvin waves (Matsuno, 1966). The geopotential height field exhibits a dipolar structure along the equator where the wind and mass fields are generally balanced in the meridional direction and unbalanced in the zonal direction. This feature is not clearly seen in the total fields (Fig. 4). In EXP_POS, the winds converge towards the warm area along the equator at the lower level (Fig. 5a), whereas at the upper level the winds flow zonally away from the area (Fig. 5b). EXP_NEG has similar bias patterns to EXP_POS, but with opposite signs and smaller magnitudes (Figs. 5c and 5d). In EXP_IOD (Figs. 5e and 5f), the Kelvin-type

295 biases shift a bit westward compared with EXP_POS.
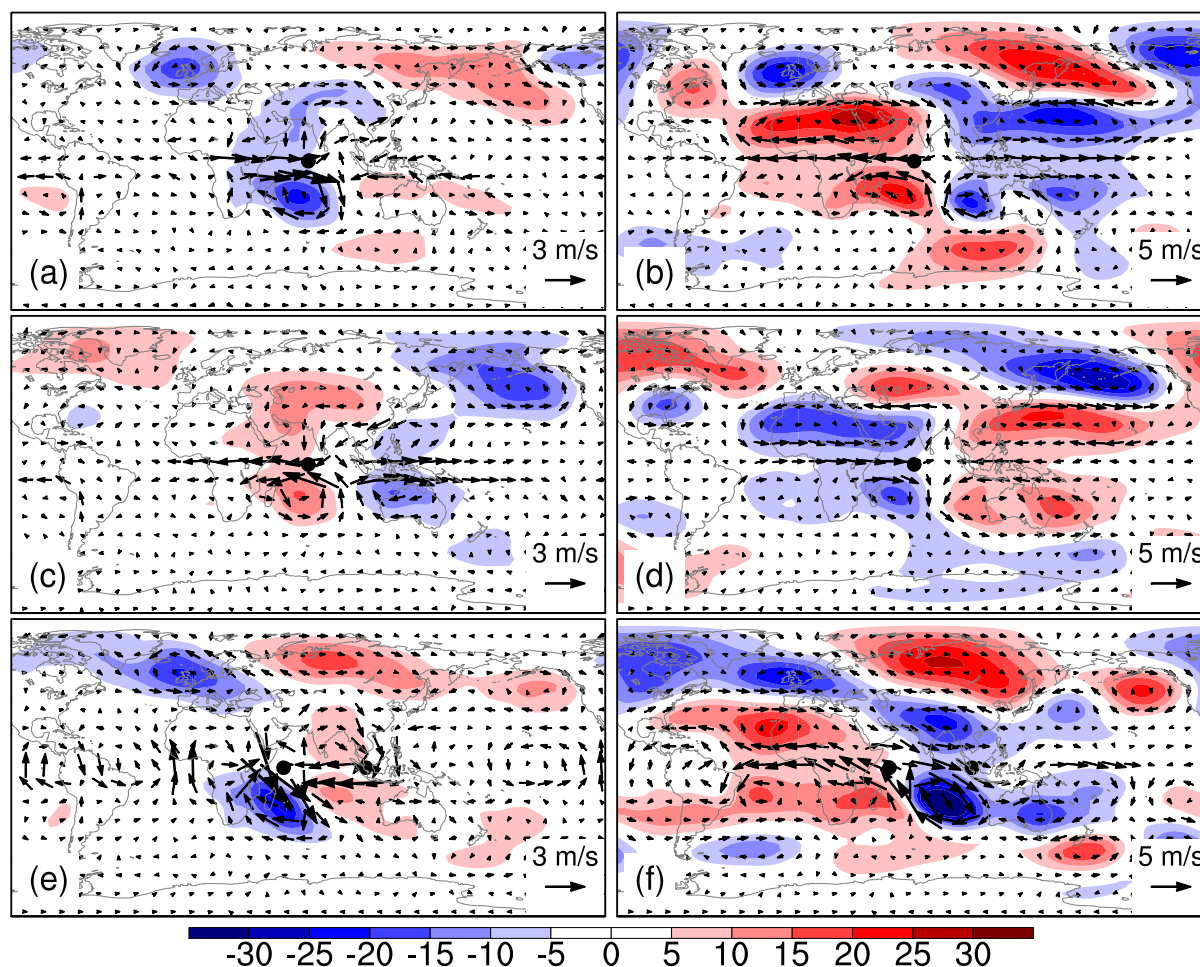
Figure 6. Same as Fig. 5, but for the balanced wave circulation biases.

Figure 6 shows the balanced circulation biases. They also share a number of common features among the four experiments. The bias fields are characterized by a quadrupole in the tropics and subtropics (referred to from now on as TROP). In the

extratropics (referred to from now on as EXTR), alternatively distributed cyclones and anticyclones organized in stationary
Rossby wave-train-like pattern are observed. Vertically, the TROP biases are baroclinic, similar to their unbalanced counterparts
300 (Fig. 5). In contrast, the EXTR biases are generally barotropic. The biases in EXP_POS (Figs. 6a and 6b) and EXP_NEG (Figs.
6c and 6d) have similar patterns but with opposite signs. In extratropics, strong biases are particularly seen in the PNA region.
Although EXP_IOD adopts a dipolar SST bias, its TROP bias fields are largely defined by the positive SST bias. The circulation
bias centers in EXP_IOD overall shift westward compared to the other experiments (Figs. 5e and 5f). This is consistent with
previous studies that the atmospheric response to a dipolar heating in the tropics is mostly defined by the positive heating
305 anomaly (Kosovelj et al., 2019). In contrast to the other experiments, the EXTR biases in EXP_IOD are strong over North
America and Eurasia but relatively weak over North Pacific (Fig. 6f).

3.3.3 Bias teleconnections

The TROP and EXTR balanced biases are connected to each other and this can be demonstrated by using the the stationary
wave activity flux (WAF; Plumb, 1985) and the Rossby wave source (RWS; Sardeshmukh and Hoskins, 1988). The WAF
310 is an indicator of the propagation of the Rossby wave activity. The RWS denotes the wave forcing and it takes the form
$-\nabla \cdot \mathbf{v}_\chi (\zeta + f)$, where $\mathbf{v}_\chi$ represents the divergent wind, ζ the relative vorticity and f the Coriolis parameter. Positive (negative)
RWS indicates cyclonic (anticyclonic) wave forcing. The bias-related WAF and RWS are evaluated at 250 hPa. In the evaluation
of WAF, the stationary wave fields are referred to as the 80-year averaged balanced circulation biases with the zonal-mean
part removed. The RWS bias is computed as the time-mean difference between the RWS of the sensitivity and the reference
315 simulations.

The maps of RWS and WAF associated with biases in DJF are displayed in Fig. 7. The major feature is the wave propaga-
tion indicated by WAF over East Aisa and the PNA region. EXP_POS and EXP_NEG have similar wave propagation which
first spreads northeastward from the subtropical central Pacific, then eastward across the north America, north Atlantic, and
finally terminates over north Africa (Figs. 7a and 7b). The wave-train in EXP_IOD originates from south Asia. It first spreads
320 northeastward and then eastward across the north Pacific (Fig. 7c). The wave route in EXP_IOD is much zonal, which may be
due to the wave being trapped by the jet stream (Zhang and Liang, 2022).

In addition, one can see that the wave propagation in all experiments originates from the subtropics where RWS is strong. The
strong RWSs first generate the systems in the subtropics, which then disperses northeastward. For instance, over mid-to-east
Asia, cyclonic (anticyclonic) circulations always correspond to some positive (negative) RWSs. These strong RWSs are closely
325 related to the subtropical jet (see Fig. 2c) where there is strong vorticity gradient and the RWS can be effectively produced
through the vorticity advection by divergent wind $[-\mathbf{v}_\chi \cdot \nabla (\zeta + f)]$. This is consistent with the conventional understanding of
the teleconnection induced by tropical heating (e.g., Trenberth et al., 1998).

3.3.4 Separation of tropical and extratropical biases in balanced circulation

This section aims at separating the TROP and EXTR balanced biases which, implied by their vertical structures, have different
330 origins and dynamics. The separation is performed in the modal space with the aid of the Z profiles (the third component of
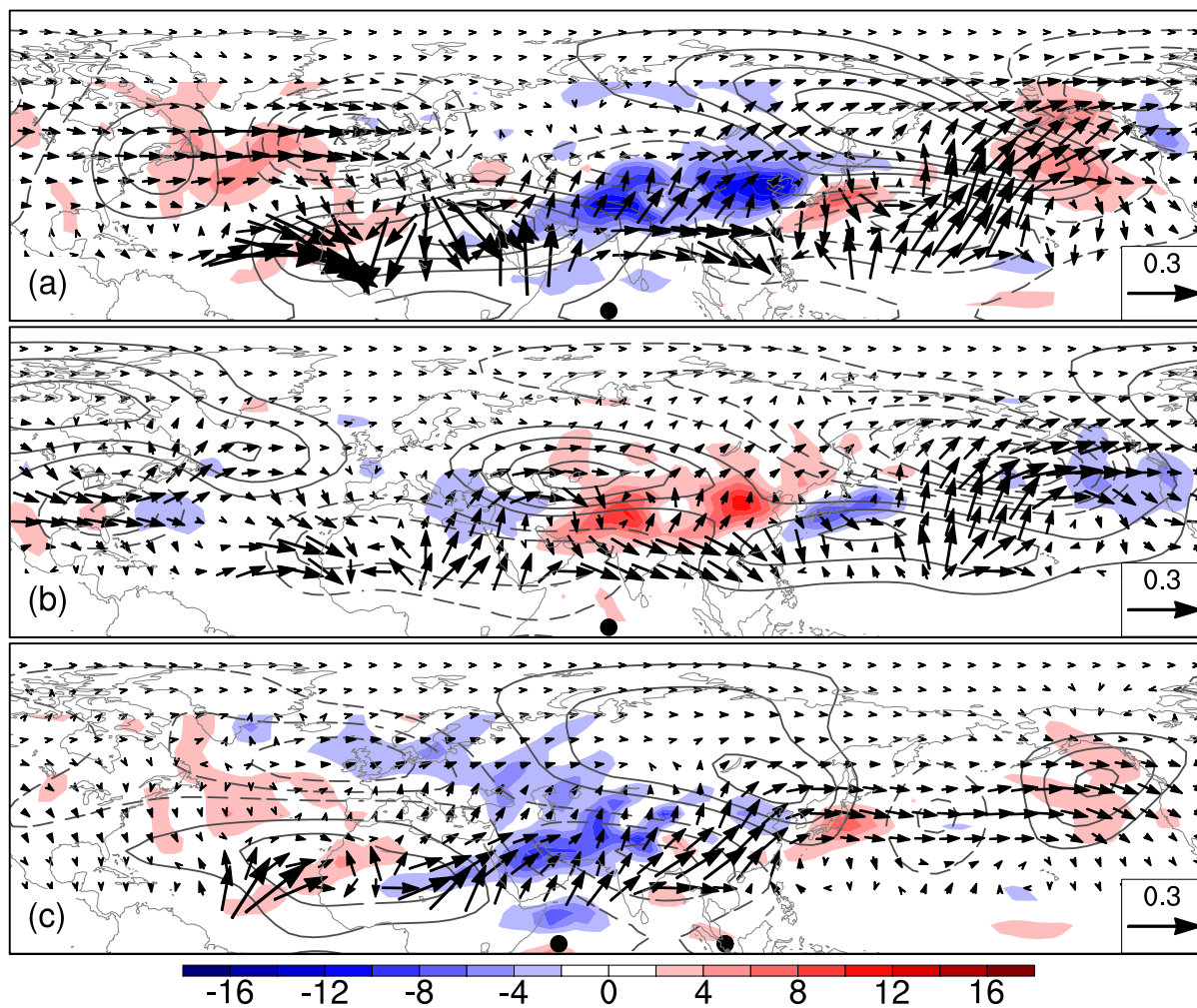
Figure 7. Horizontal distribution of the 250 hPa stationary wave activity flux (vectors, $m^2\ s^{-2}$) and Rossby wave source (colors, $10^{-11}\ s^{-2}$) in DJF: (a) EXP_POS, (b) EXP_NEG and (c) EXP_IOD. Black contours show the balanced geopotential height biases. The contour interval is 5 gpm. Negative values are indicated with dashed lines and the zero-line is omitted.
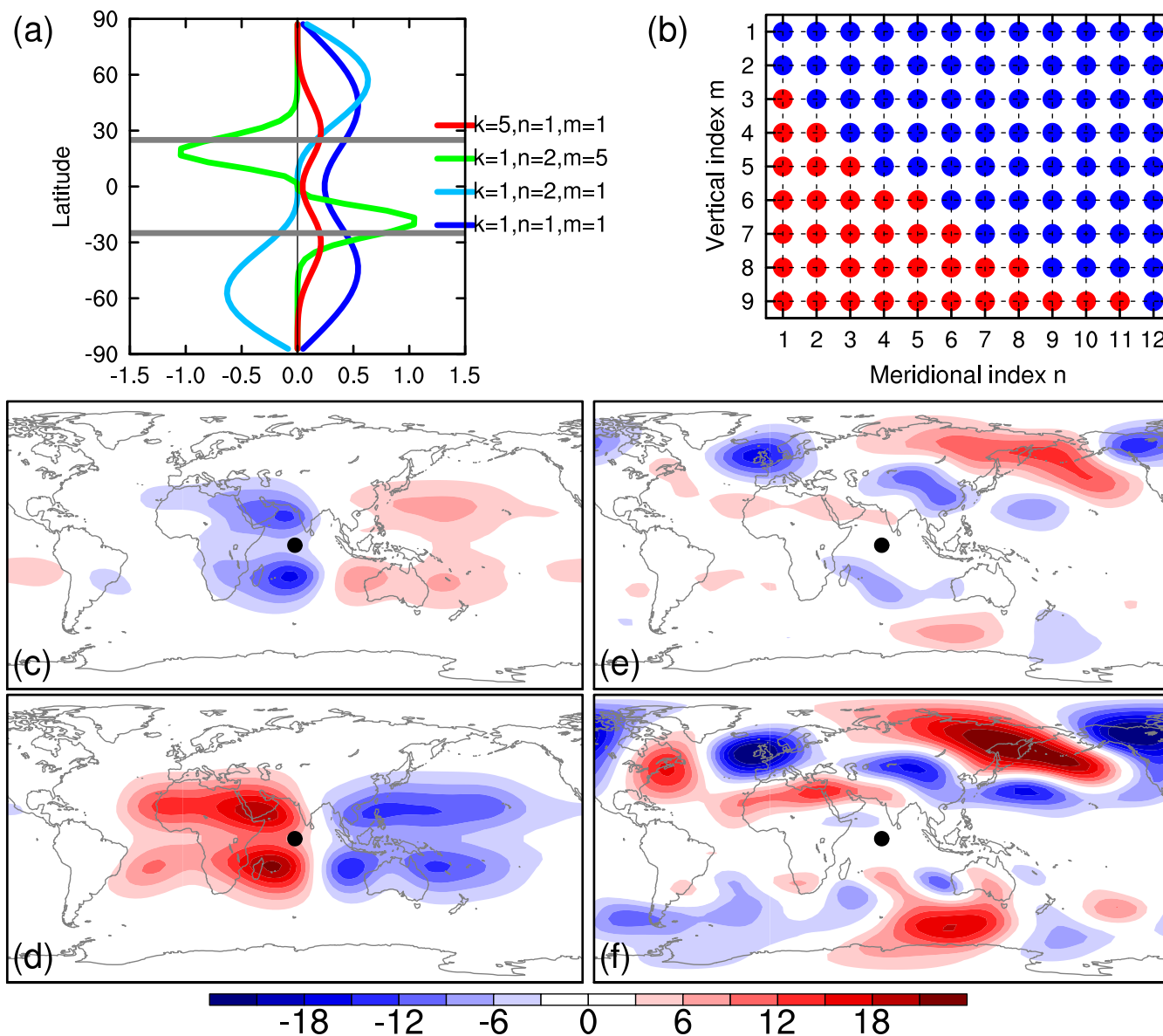
Figure 8. (a) Examples of the Rossby mode Z profiles. Gray lines mark the latitudes $\pm 25°$. (b) Classification of the TROP and EXTR modes in modal space at zonal wavenumber $k = 1$ based on Z profiles. Red (blue) dots denote the TROP (EXTR) modes. (c-d) Reconstructions of the DJF TROP balanced geopotential height biases (m) in EXP_POS at (c) $\sigma = 0.924$ and (d) $\sigma = 0.211$. (e-f) Same as (c-d), but for the EXTR biases.

$\mathbf{H}_n^k(\varphi; m)$). Although NMFs are global functions, they do have local features. Figure 8a displays some meridional profiles of Z of the Rossby modes. One can see that the structure of Z depends on the mode index $\nu = (k, n, m)$. In general, the Z maxima (or minima) shift equatorward with m and k and move poleward with n. The latitude of Z maximum (or minimum) indicates the action center of the Rossby modes. In this study, we classify the Rossby mode that has its Z maximum (or minimum) located between 25° S and 25° N into the TROP modes, otherwise we put it in the EXTR modes. We also used latitude $\pm 30°$ as the separation criterion and got the same results.

Figure 8b shows the separation in the meridional and vertical mode index plane at zonal wavenumber $k = 1$. We see that all modes with vertical mode index $m = 1$ or 2 (namely the tropospheric barotropic modes) are recognized as the EXTR modes, consistent with the observations that the extratropical Rossby waves are generally barotropic (see Fig. 6). But note that the extratropical biases are not purely barotropic. As the meridional mode index n increases, baroclinic modes go into the EXTR regime. Also note that the structure of Z depends on k as well, but it changes slowly with k. Indeed, the separations are almost identical among zonal wavenumbers $k < 7$ (not shown). Finally, 1337 TROP modes and 6493 EXTR modes are recognized (the zonal-mean modes and MRG modes are excluded in the classification). The TROP and EXTR balanced circulation biases are then reconstructed with the Hough coefficients of the corresponding categories.

The reconstructed TROP and EXTR balanced circulation biases in DJF from EXP_POS are shown in Figs. 8c-8f. As expected, the TROP biases are confined in the tropics which are characterized by equatorial baroclinic Rossby waves (Figs. 8c and 8e). The EXTR biases are dominated by mid-to-high latitude barotropic systems, and the tropical signals are very weak (Figs. 8c and 8d). Nevertheless, there is no clear geographical boundary between the TROP and EXTR biases. The TROP-EXTR separation can benefit us in understanding the impacts of these biases on the spatio-temporal variability.

3.4 Bias and variance quantification

In this section, we first look at the impact of the biases on the simulated spatio-temporal variability in the spectral space, followed by a discussion in physical space. As previously elucidated, while the total energy (kinetic energy plus potential energy) remains conserved under weak SST biases, the available potential energy, as well as the kinetic energy, do not.

3.4.1 Variance budget in modal space

Let us first discuss the overall energy budget. Figure 9 shows the changes of time-mean energy ($\Delta \overline{I}$), climatological energy (ΔE) and temporal variance (ΔV). Since the DJF-mean fields are used in the computation, the temporal variance V indicates the interannual variability. These quantities have been computed separately for the zonal-mean modes ($k = 0$) and the wave modes ($k > 0$) and the balanced wave modes are further divided into the TROP and the EXTR components. Positive (negative) value means increase (decrease) of the energy or variance with respect to the reference simulation. One can find that $\overline{I}$ and E have similar changes regardless of regimes, implying E dominates V in the $\overline{I}$ budget. As for the zonal-mean ($k = 0$) modes, they decrease in the unbalanced part (Fig. 9a) and increase in the balanced part (Fig. 9b) in all experiments. The overall changes vary with experiments but their magnitudes are generally smaller than 5% of the reference. As for the wave ($k > 0$) modes, the unbalanced $\overline{I}$ and E increase in all experiments except EXP_IOD (Fig. 9c), similar to that of the TROP balanced modes
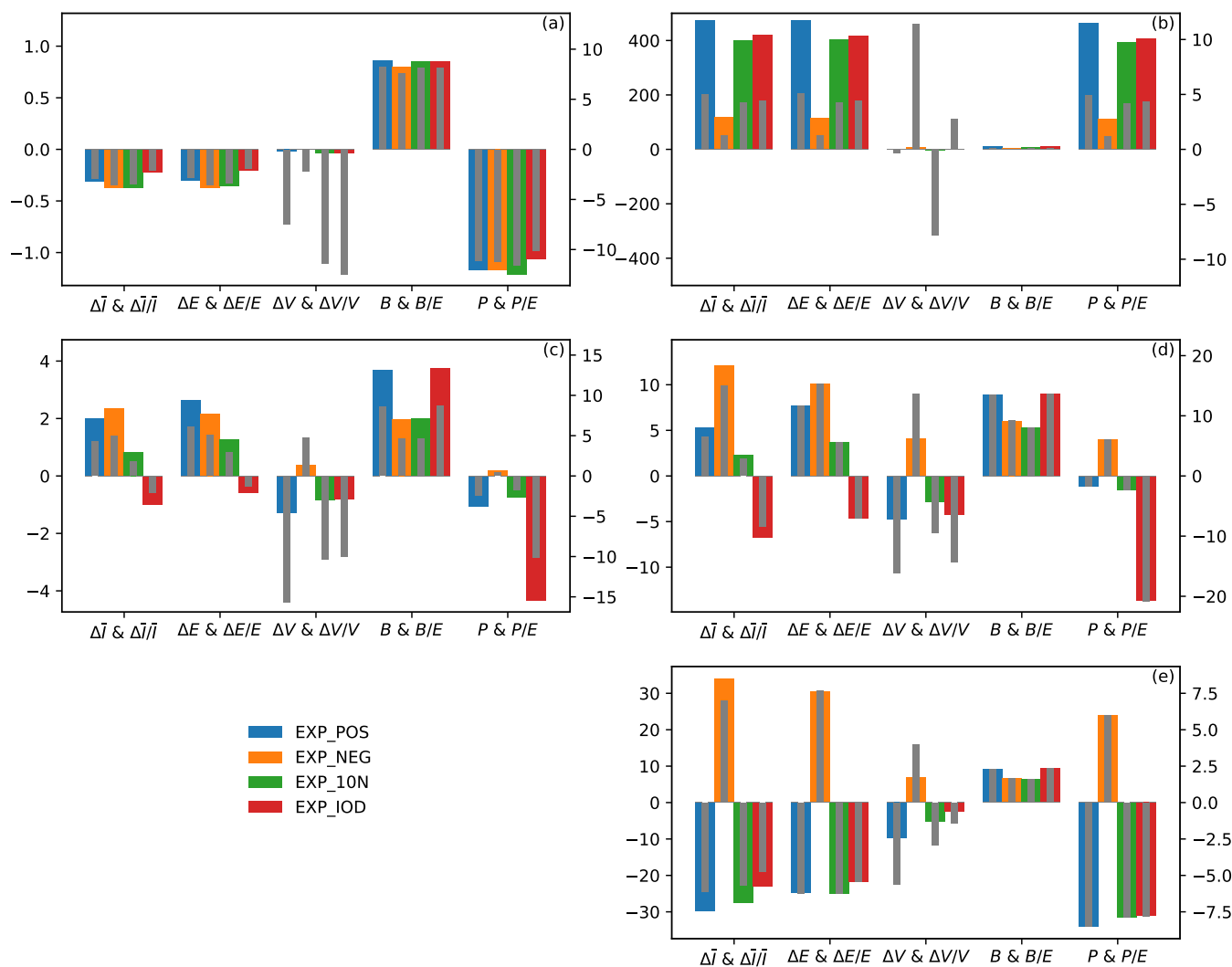
Figure 9. Absolute (wide bars) and relative (narrow bars) changes of the total energy and the interannual variance. The left panels show the results of the unbalanced (a) zonal-mean modes ($k = 0$) and (c) wave modes ($k > 0$). The right panels show the results of the (b) balanced zonal-mean modes ($k = 0$), (d) TROP balanced wave modes ($k > 0$) and (e) EXTR balanced wave modes ($k > 0$). The relative change is calculated as the absolute change divided by the corresponding reference state. The left ordinate gives the magnitude of the absolute changes (in m^2 s^{-2}) and the right ordinate gives that of the relative changes (in %).

(Fig. 9d). It is not surprising to see the similarity between the changes of these two wave species since the Kelvin modes
which dominate the unbalanced flow and the equatorial Rossby modes which dominate the TROP balanced flow form a whole
response to a tropical heating (Matsuno, 1966; Gill, 1980) and therefore they are in phase. Regarding the EXTR balanced
modes, $\overline{I}$ and E decrease in all experiments except EXP_NEG where they increase (Fig. 9e). The magnitudes of the relative
changes in the unbalanced wave energy are generally smaller than 5% (Fig. 9c), and those in the TROP balanced wave energy
range from 3% (EXP_10N) to 15% (EXP_NEG) (Fig. 9d). The relative changes of the EXTR balanced wave energy stay
around 5% in all experiments (Fig. 9e).

The energy changes can be further understood through B and P terms, the two components of ΔE. One can see that
P dominates B in the zonal-mean modes (Figs. 9a and 9b) and the EXTR balanced wave modes (Fig. 9e). In contrast, B
dominates P in the unbalanced wave modes (Fig. 9c) and the TROP balanced wave modes (Fig. 9d) except EXP_IOD where
the opposite situation happens. This indicates that energy changes in the zonal-mean modes and the EXTR balanced wave
modes are mainly attributed to the covariance between bias and the reference state (i.e., bias phase) and energy changes in
other modes are largely determined by bias magnitude. In addition, P is negative in the unbalanced zonal-mean modes and
EXTR balanced modes (except EXP_NEG) indicating large phase bias ($|\Delta\theta| > \pi/2$), whereas it is generally positive in the
other modes indicating relatively small phase bias ($|\Delta\theta| < \pi/2$).

Regarding V, it decreases in the unbalanced zonal-mean ($k = 0$) mode in all experiments (Fig. 9a). For the balanced zonal-
mean ($k = 0$) mode, V increases in EXP_NEG and EXP_IOD and decreases in the other two experiments (Fig. 9b). For the
wave modes of all kinds, V decreases in all experiments except EXP_NEG where it increases (Figs. 9c-9e), implying that
positive (negative) TIO SST bias weakens (strengthens) the global interannual variability of the wave flow. Although ΔV in
the zonal-mean flow is very small compared with $\Delta\overline{I}$ and ΔE, the relative change $\Delta V/V$ could be large. It can be over 10%
in the zonal-mean modes as well as the TROP wave modes (Figs. 9a-9d). Comparisons among experiments indicate that the
TIO SST bias has relatively stronger influence on V in the tropics (Figs. 9c and 9d) than in the extratropics (Fig. 9e) in terms
of their relative changes.

The climatological energy change ΔE with respect to k is displayed in Fig. 10, which is similar to $\Delta\overline{I}$ (not shown). We first
look at the unbalanced regime (Figs. 10a-10c). One can find that the mode $k = 1$ dominates the energy change in EXP_POS and
EXP_10N (Fig. 10a), which is largely due to the B term (Fig. 10b). In EXP_NEG, it is the modes $k = 1$ and 2 that dominate
the energy change, which originates from both B and P terms (Fig. 10c). In EXP_IOD, the modes $k = 1-3$ dominate, and the
energy change is mostly determined by P which is negative in modes $k = 1$ and 2 and positive in mode $k = 3$ (Fig. 10d). This
implies large phase difference between the reference state and the circulation bias of modes $k = 1$ and 2 caused by the dipolar
SST bias. Regarding the balanced regime, the TROP component has similar spectra to the unbalanced regime in terms of ΔE,
B and P (Figs. 10d-10f). This has been explained in preceding parts. As for the EXTR component, ΔE is dominated by the
mode $k = 1$ in all experiments (Fig. 10g), which is predominately due to the P term (Fig. 10i).

Another point worth noting is the spectra of B term, which indicates the circulation bias strength (Figs. 10b, 10e, 10h). They
seem to decay exponentially with k. Quantitative calculations (Table 2) show that 90-95% bias variance is stored in the first 6
zonal modes ($k = 0-5$), consistent with Žagar et al. (2020) that the representation of the SST is crucial for the planetary scales.
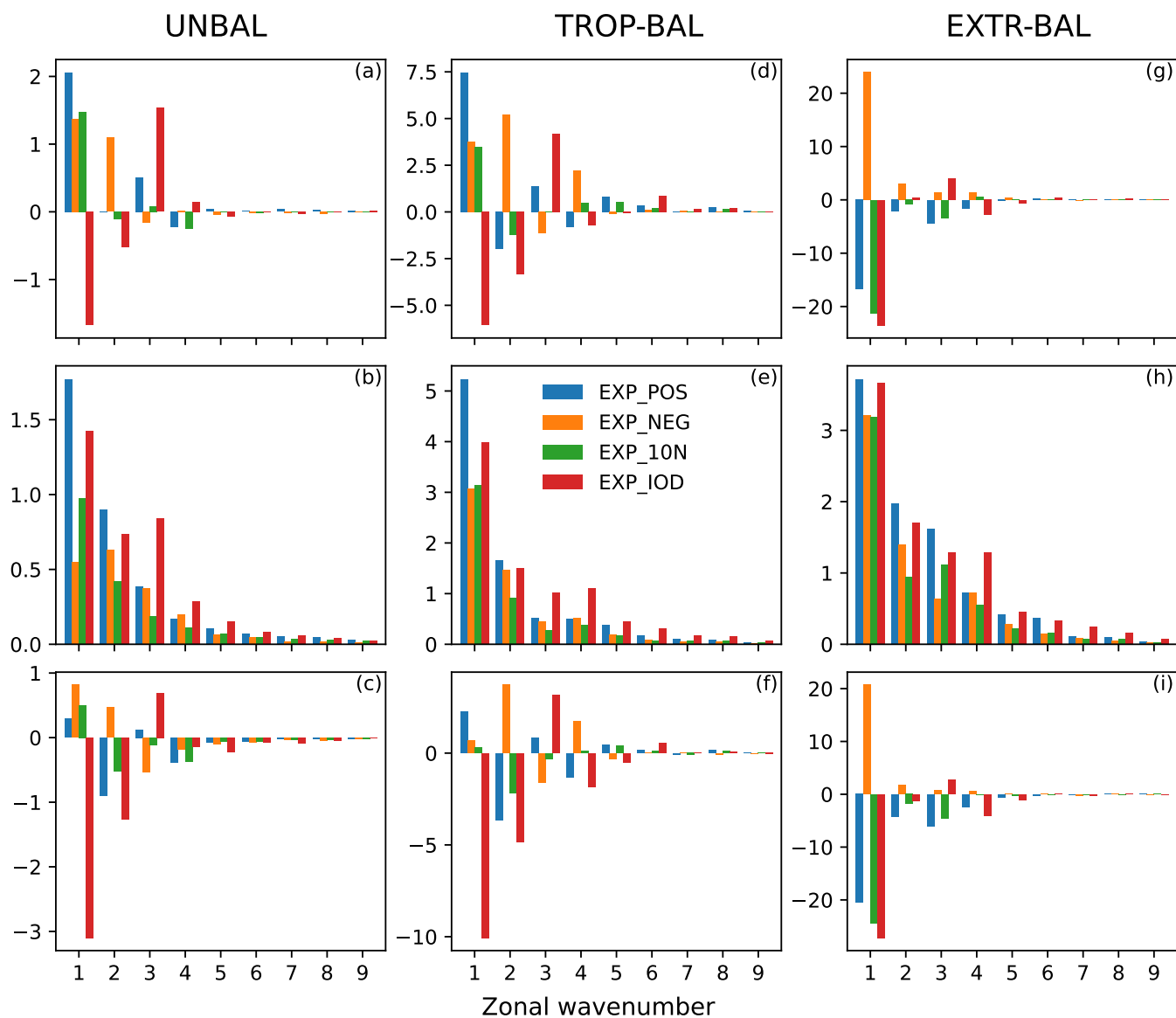
Figure 10. (left column) The spectra (in m^2 s^{-2}) of (a) ΔE, (b) B and (c) P as a function of zonal wavenumber k for the unbalanced modes, which have been summed over the meridional index n and the vertical index m. (middle column) The same as left panels, but for TROP balanced modes. (right column) The same as left panels, but for EXTR balanced modes.

Table 2. Bias variance and the percentages of selected modes in DJF. The percentage is calculated as the bias variance of the selected modes divided by the corresponding total bias variance (including $k = 0$).

Experiments	EXP_POS		EXP_NEG		EXP_10N		EXP_IOD	
Regimes	UNBAL	BAL	UNBAL	BAL	UNBAL	BAL	UNBAL	BAL
Total variance (J kg^{-1})	4.6	28.2	2.8	16.6	2.9	20.8	4.6	28.9
$k = 0$ (%)	19.0	35.9	28.7	23.4	29.9	43.5	18.6	36.5
$k = 1\text{-}5$ (%)	73.3	59.5	65.2	72.3	61.6	52.7	74.6	57.1
$m = 1\text{-}2$ (%)	10.9	24.8	16.6	28.0	16.5	28.5	11.0	29.3
$m = 3\text{-}4$ (%)	65.5	49.1	53.2	44.8	59.3	40.8	70.9	47.0
Symmetric modes (%)	88.1	77.1	83.2	73.2	83.0	73.6	87.9	73.6
Kelvin (%)	64.7	-	51.7	-	49.7	-	65.7	-
MRG (%)	-	0.8	-	0.91	-	0.7	-	1.0

Besides, a large part (ranging from 73% to 88%) of the bias variance comes from the meridional symmetric modes which in
400 the unbalanced regime are dominated by the Kelvin modes, and the MRG modes contribute less than 1% to the balanced bias
variance. This is even true in EXP_10N where the erroneous SST forcing is situated north of the equator. Furthermore, more
bias variance comes from the baroclinic modes ($m = 3$ and 4) than the barotropic modes ($m = 1$ and 2). On the other hand,
different SST biases result in different amounts of bias variance. For instance, EXP_POS and EXP_IOD have similar amount
of bias variance, stronger than the other two experiments.
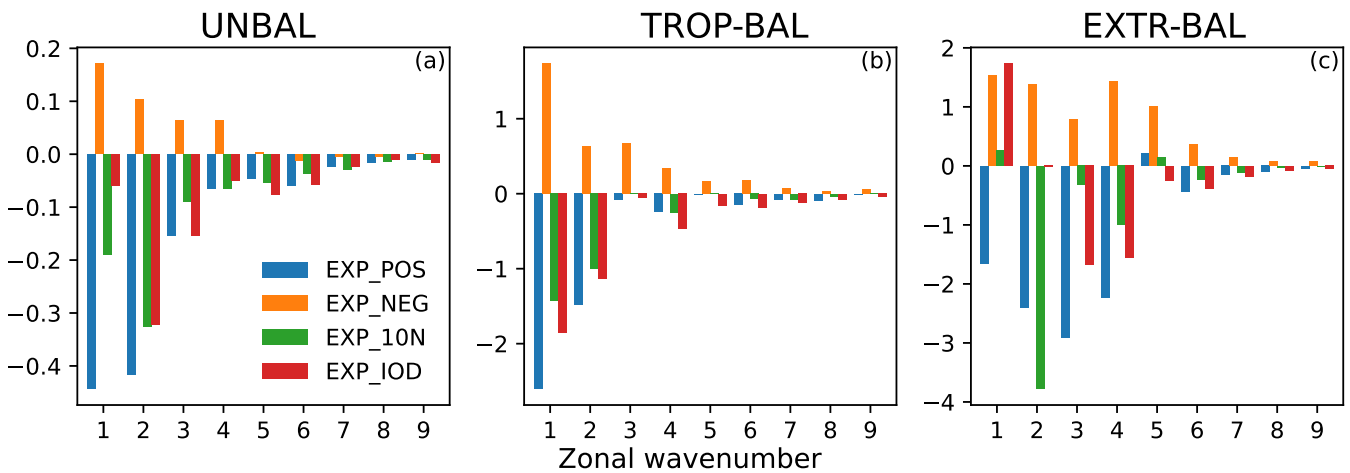
Figure 11. (left) The spectra (in m^2 s^{-2}) of ΔV as a function of zonal wavenumber k for (a) the unbalanced modes, (b) the TROP balanced
modes and (c) the EXTR balanced modes. The results have been summed over the meridional index n and the vertical index m..

405 The interannual variance (IAV) change ΔV with respect to k is displayed in Fig. 11. In contrast to ΔE, more zonal modes
engage in ΔV. Visible changes are seen at large zonal wavenumbers. The unbalanced regime (Fig. 11a) and the TROP bal-
anced regime (Fig. 11b) have similar spectrum structures, albeit with different magnitudes. The modes $k = 1 - 2$ dominate in

EXP_POS and EXP_10N and the modes $k = 1 - 4$ dominate in EXP_NEG. A difference was seen in EXP_IOD, where ΔV is dominated by modes $k = 2$ and 3 in the unbalanced regime whereas by modes $k = 1$ and 2 in the TROP balanced regime.

410 The ΔV spectra in the EXTR balanced regime differs (Fig. 11c). One can see that ΔV is dominated by modes $k = 1 - 4$ in EXP_POS, by modes $k = 1 - 5$ in EXP_NEG, and by modes $k = 2$ and 4 in EXP_10N. In EXP_IOD, the modes $k = 1$, 3 and 4 dominate, but with different signs. The mode $k = 1$ is positive whereas the other two are negative, which define the total change.
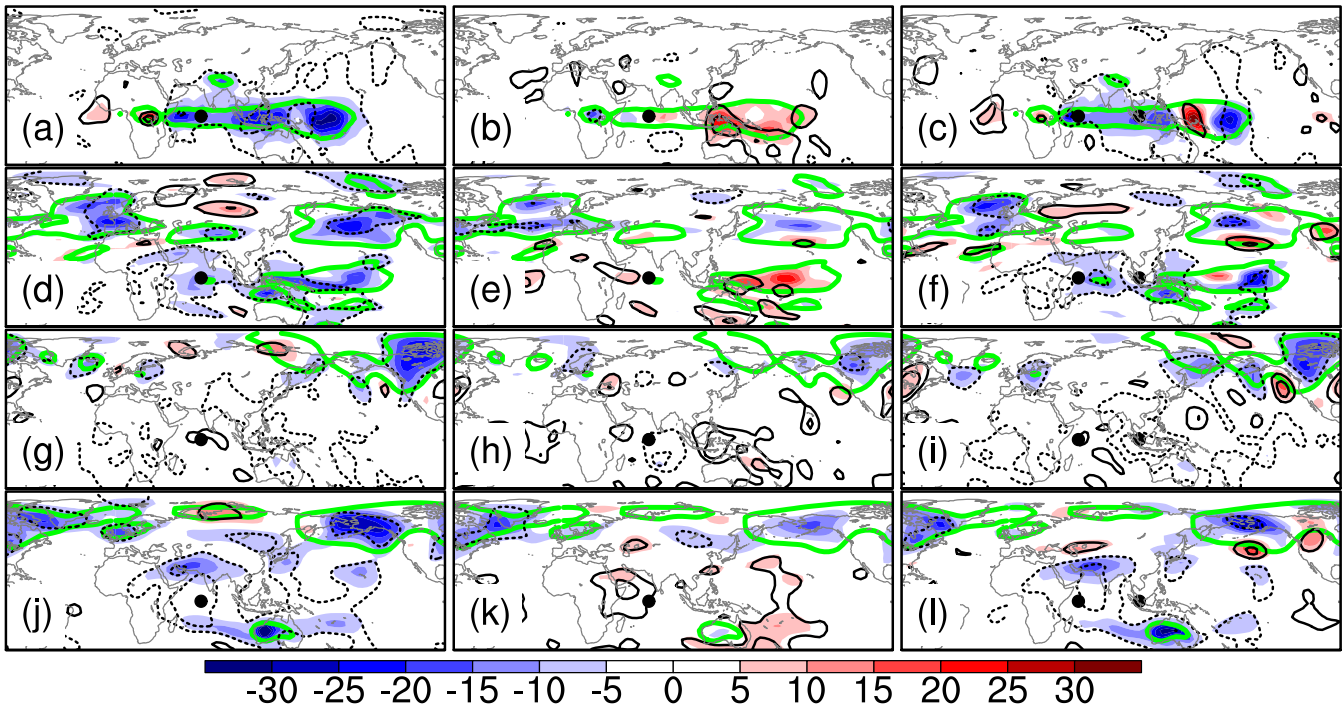
Figure 12. Absolute changes (colors; in m^2 s^{-2}) and relative changes (black contours; in %) of the interannual variance (which have been summed over the vertical index m, namely $\sum_m S_m$) in DJF with respect to the reference simulation: (top row) unbalanced zonal wind, (second row) balanced zonal wind, (third row) balanced meridional wind and (bottom row) balanced geopotential height. Left column shows the results from the EXP_POS, middle column those from the EXP_NEG, and right column those from the EXP_IOD. The zonal-mean modes are absent in the variance computation. The absolute changes in panels (a)-(c) have been multiplied by 10 to facilitate drawing. Black contour levels ±25% and ±50% are drawn; negative values are indicated with dashed lines. Thick green contours show the corresponding mean reference at levels (a-c) 3, (d-f) 30, (g-i) 30 and (j-l) 40 m^2 s^{-2}, respectively.

3.4.2 Interannual variance changes in physical space

415 The horizontal distribution of the interannual variance (IAV) changes is displayed in Fig. 12. The IAV is computed based on the fields after the vertical projection (Eq. (13)). EXP_10N have similar distributions to EXP_POS and are thus not shown. Generally speaking, strong IAV changes are seen in regions where the background IAV is strong, and the distributions of the

IAV changes do not have large differences among experiments. In the unbalanced regime, the IAV changes are dominated by the zonal wind (Figs. 12a-12c) and the geopotential height (not shown), which have similar IAV changes in terms of structure

420 and magnitude. In the unbalanced zonal wind, strong IAV changes are confined in low latitudes, especially in the Indo-west Pacific region, the equatorial Atlantic and Africa, south Asia and Australia, where the IAV changes can be over 25% of the reference.

In the balanced regime, strong IAV changes are seen globally (Figs. 12d-12l). In low latitudes, both zonal wind and geopotential height have strong IAV changes, but with different distributions. In the zonal wind, the IAV change centers are distributed

425 along the equator in the Indo-west Pacific region (Figs. 12d-12f), whereas in the geopotential height the IAV change centers are seen in subtropics, such as Middle East, south Asia, Australia and subtropical central Pacific (Figs. 12j-12l). In the meridional wind, though the absolute IAV changes are weak in the tropics, its relative changes can be large (over 25%), especially in the TIO region and the Maritime Continent (Figs. 12g-12i). In mid-to-high latitudes, strong IAV changes generally happen in the PNA sector, north Atlantic and Europe, although the locations of the change centers vary with variables. In the zonal wind,

430 the IAV change centers are mostly seen in midlatitudes, over the north Pacific and to the west of Europe (Figs. 12d-12f). In the meridional wind, the IAV change centers are confined in high latitudes, especially over Canada, Alaska and northeast Asia (Figs. 12g-12i). The IAV changes of the geopotental height are large over Alaska, eastern North America, north Europe and northeast Asia (Figs. 12j-12l). The IAV changes in the extratropics should be attributed to the impact of the balanced biases on wave and zonal-mean flow interaction (see Fig. 7). The balanced biases (i.e., stationary Rossby waves) could modify the

435 background flow (e.g., jet stream), which in turn affects the nonlinear interaction between them, leading to variations of both energy and interannual variability (e.g., Lau and Nath, 1991; Wettstein and Wallace, 2010; Zhao and Liang, 2018).

4 Conclusions and outlook

We investigated remote effects of regional SST bias in the tropical Indian Ocean (TIO) region using century long (1901-2010) simulations. Motivated by results from CMIP5 and CMIP6 simulations, the SST biases were prescribed as monopole

440 or dipole anomalies in the TIO region superimposed on the SST from ERA20C reanalyses with maximal amplitudes of ± 1.5 K. Systematic SST errors enter the atmosphere through the moisture and heat fluxes thereby affecting local precipitation, and generating local and remote changes in the circulation. These effects are termed "bias teleconnections". While simplified with respect to the real atmosphere and coupled climate models, the application of intermediate complexity model with prescribed SST provides a framework for understanding changes in multiannual spatio-temporal variability associated with systematical

445 errors in regional SST.

First of all, we asked about the spatial structure of circulation biases in simulated circulation in the tropics and extratropics. The results show that the bias structure caused by the TIO SST biases is similar to the steady state response to tropical diabatic heating. Although it depends on the sign and location of the SST bias, the induced circulation bias generally has the Gill-Matsuno-type pattern in the tropics and Rossby wave-train distribution in the extratropics, especially in the Pacific-North

450 American (PNA) sector. In addition, the circulation biases are mainly recognized at planetary scales, with over 90% of bias

variance (proportional to the second moment of the time-mean difference of Hough coefficients between the sensitivity and reference simulations which represents the circulation bias in modal space; see Eq. (18)) stored in the zonal mean state (zonal wavenumber $k = 0$) and large scales ($k = 1 - 5$). This is consistent with Žagar et al. (2020) who found that the SST bias has the largest impact on planetary scales at climate timescales.

455   Our second question was about the dynamical mechanisms that connect the TIO SST bias to biases in simulated circulation. As we showed, the circulation bias in the tropics results from the linear response of the atmosphere to the TIO SST bias and its connection with the extratropical bias is set up by Rossby wave-train emanating from the subtropical areas with strong Rossby wave sources.

The third major question posed was about changes in the atmospheric energy and the interannual variability in response 460   to the TIO SST biases. With regard to the zonal-mean-flow energy, we found that the unbalanced part decreases, while the balanced part increases across all experiments. These changes primarily arise from the covariance between the bias and the reference state (i.e., the P term). For the wave-flow energy, the unbalanced part and the tropical balanced part change in phase, increasing in all experiments except that with the IOD-type SST bias (EXP_IOD), where it decreases. In experiments where a positive SST bias is located at the equator (EXP_POS) or at $10°$ N (EXP_10N), the energy changes in mode $k = 1$ 465   dominate, which are largely due to the bias variance (i.e., the B term). In experiment with a negative SST bias located at the equator (EXP_NEG), modes $k = 1$ and $k = 2$ dominate, and the energy changes come from both B and P terms. In EXP_IOD, modes $k = 1$ to $k = 3$ dominate, and the energy change is largely determined by P term. In contrast, the extratropical balanced wave-flow energy decreases in all experiments except EXP_NEG, where it increases. Changes in the extratropical balanced wave-flow energy are mainly attributed to the P term.

470   The changes in interannual variance (IAV) is contingent upon the sign of the SST bias. Positive and negative SST biases in TIO have opposite effects on the interannual variability. We found that a positive SST bias results in a reduction of up to 15% in the IAV of the unbalanced wave flow, up to 16% in the tropical balanced wave flow, and up to 6% in the extratropical balanced wave flow, when compared to the reference state. Conversely, a negative SST bias produces the opposite results, increasing the IAV of the unbalanced wave flow by approximately 5%, and that of the tropical and extratropical balanced wave 475   flow by up to 14% and 4%, respectively. In addition, in contrast to the energy response, more zonal modes engage in the IAV response. Visible IAV changes are seen at larger zonal wavenumbers. Geographically, the IAV responses to the TIO SST bias are predominantly confined to the Indo-west Pacific region, Australia, south and northeast Asia, the Pacific-North America region and Europe, where the background interannual variability is strong.

Our numerical experiments were conducted using an atmosphere-only GCM forced with prescribed SST. Therefore, there is 480   only forcing of the atmosphere from the SST but with no feedback from the atmosphere to the ocean. While this simplifies the problem under study, it reduces the reality of simulated processes in the TIO region. In fact, the SST variability in the region is coherent with monsoon variability with a phase relation consistent with a coupled oscillation (Vecchi and Harrison, 2002), which is absent from the atmosphere-only GCM. The coupling between the SST and the precipitation (deep convection) could therefore be more complicated than depicted in this study. On the other hand, SST biases in CMIP models persist in many

485   other regions (Wang et al., 2014; Zhang et al., 2023). In future studies, we will extend the approach developed in this study to other regional oceans to quantify the sensitivity of the atmospheric bias teleconnections to the location of the SST bias.

Code and data availability. All data used in this work can be obtained from Y.-B. Zhao through email. The PLASIM source code and detailed userguide can be downloaded at https://www.mi.uni-hamburg.de/en/arbeitsgruppen/theoretische-meteorologie/modelle/plasim.html. The MODES package can be requested via https://modes.cen.uni-hamburg.de.

490   *Author contributions.* YBZ and NŽ designed the study and YBZ carried them out. All co-authors contributed to interpreting the results. YBZ prepared the manuscript with contributions from all co-authors.

Competing interests. The authors declare that they have no conflict of interest.

Acknowledgements. This work is a contribution to project S1 of the Collaborative Research Centre TRR 181 "Energy Transfer in Atmosphere and Ocean" funded by the Deutsche Forschungsgemeinschaft (DFG, German Research Foundation) under project number 274762653.

References

Annamalai, H., Okajima, H., and Watanabe, M.: Possible Impact of the Indian Ocean SST on the Northern Hemisphere Circulation during El Niño, Journal of Climate, 20, 3164–3189, https://doi.org/10.1175/JCLI4156.1, 2007.

Annamalai, H., Taguchi, B., McCreary, J. P., Nagura, M., and Miyama, T.: Systematic Errors in South Asian Monsoon Simulation: Importance of Equatorial Indian Ocean Processes, Journal of Climate, 30, 8159–8178, https://doi.org/10.1175/JCLI-D-16-0573.1, 2017.

Back, L. E. and Bretherton, C. S.: On the Relationship between SST Gradients, Boundary Layer Winds, and Convergence over the Tropical Oceans, Journal of Climate, 22, 4182–4196, https://doi.org/10.1175/2009JCLI2392.1, 2009.

Bai, H., Li, B., Mehra, A., Meixner, J., Moorthi, S., Ray, S., Stefanova, L., Wang, J., Wang, J., Worthen, D., Yang, F., and Stan, C.: The impact of tropical SST biases on the S2S precipitation forecast skill over the Contiguous United States in the UFS global coupled model, Weather and Forecasting, in press, https://doi.org/https://doi.org/10.1175/WAF-D-22-0162.1, 2023.

Beal, L. M., Vialard, J., Roxy, M. K., Li, J., Andres, M., Annamalai, H., Feng, M., Han, W., Hood, R., Lee, T., Lengaigne, M., Lumpkin, R., Masumoto, Y., McPhaden, M. J., Ravichandran, M., Shinoda, T., Sloyan, B. M., Strutton, P. G., Subramanian, A. C., Tozuka, T., Ummenhofer, C. C., Unnikrishnan, A. S., Wiggert, J., Yu, L., Cheng, L., Desbruyères, D. G., and Parvathi, V.: A Road Map to IndOOS-2: Better Observations of the Rapidly Warming Indian Ocean, Bulletin of the American Meteorological Society, 101, E1891–E1913, https://doi.org/10.1175/BAMS-D-19-0209.1, 2020.

Bollasina, M. A. and Ming, Y.: The general circulation model precipitation bias over the southwestern equatorial Indian Ocean and its implications for simulating the South Asian monsoon, Climate Dynamics, 40, 823–838, https://doi.org/10.1007/s00382-012-1347-7, 2013.

Cai, W. and Cowan, T.: Why is the amplitude of the Indian Ocean Dipole overly large in CMIP3 and CMIP5 climate models?, Geophysical Research Letters, 40, 1200–1205, https://doi.org/10.1002/grl.50208, 2013.

Castanheira, J. M. and Marques, C. A. F.: Biases of the Barotropic Atmospheric Circulation Variability in CMIP6 Models, Journal of Climate, 35, 5071–5085, https://doi.org/10.1175/JCLI-D-21-0581.1, 2022.

Eliassen, E., Machenhauer, B., and Rasmusson, E.: On a numerical method for integration of the hydrodynamical equations with a spectral representation of the horizontal fields, 1970.

Fathrio, I., Iizuka, S., Manda, A., Kodama, Y.-M., Ishida, S., Moteki, Q., Yamada, H., and Tachibana, Y.: Assessment of western Indian Ocean SST bias of CMIP5 models, Journal of Geophysical Research: Oceans, 122, 3123–3140, https://doi.org/10.1002/2016JC012443, 2017.

Fraedrich, K. and Lunkeit, F.: Diagnosing the entropy budget of a climate model, Tellus A: Dynamic Meteorology and Oceanography, 60, 921–931, https://doi.org/10.1111/j.1600-0870.2008.00338.x, 2008.

Fraedrich, K., Jansen, H., Kirk, E., Luksch, U., and Lunkeit, F.: The Planet Simulator: Towards a user friendly model, Meteorologische Zeitschrift, pp. 299–304, https://doi.org/10.1127/0941-2948/2005/0043, 2005.

Gadgil, S., Joseph, P. V., and Joshi, N. V.: Ocean–atmosphere coupling over monsoon regions, Nature, 312, 141–143, https://doi.org/10.1038/312141a0, 1984.

Gill, A. E.: Some simple solutions for heat-induced tropical circulation, Quarterly Journal of the Royal Meteorological Society, 106, 447–462, https://doi.org/10.1002/qj.49710644905, 1980.

Hermes, J. C., Masumoto, Y., Beal, L. M., Roxy, M. K., Vialard, J., Andres, M., Annamalai, H., Behera, S., D'Adamo, N., Doi, T., Feng, M., Han, W., Hardman-Mountford, N., Hendon, H., Hood, R., Kido, S., Lee, C., Lee, T., Lengaigne, M., Li, J., Lumpkin, R., Navaneeth, K. N., Milligan, B., McPhaden, M. J., Ravichandran, M., Shinoda, T., Singh, A., Sloyan, B., Strutton, P. G., Subramanian, A. C., Thurston,

S., Tozuka, T., Ummenhofer, C. C., Unnikrishnan, A. S., Venkatesan, R., Wang, D., Wiggert, J., Yu, L., and Yu, W.: A Sustained Ocean Observing System in the Indian Ocean for Climate Related Scientific Knowledge and Societal Needs, Frontiers in Marine Science, 6, 2019.

535 Joseph, S., Sahai, A. K., Goswami, B. N., Terray, P., Masson, S., and Luo, J.-J.: Possible role of warm SST bias in the simulation of boreal summer monsoon in SINTEX-F2 coupled model, Climate Dynamics, 38, 1561–1576, https://doi.org/10.1007/s00382-011-1264-1, 2012.

Kosovelj, K., Kucharski, F., Molteni, F., and Žagar, N.: Modal Decomposition of the Global Response to Tropical Heating Perturbations Resembling MJO, Journal of the Atmospheric Sciences, 76, 1457 – 1469, https://doi.org/10.1175/JAS-D-18-0203.1, 2019.

Kuo, H. L.: On Formation and Intensification of Tropical Cyclones Through Latent Heat Release by Cumulus Convection., Journal of
540 Atmospheric Sciences, 22, 40–63, https://doi.org/10.1175/1520-0469(1965)022<0040:OFAIOT>2.0.CO;2, 1965.

Kuo, H. L.: Further Studies of the Parameterization of the Influence of Cumulus Convection on Large-Scale Flow., Journal of Atmospheric Sciences, 31, 1232–1240, https://doi.org/10.1175/1520-0469(1974)031<1232:FSOTPO>2.0.CO;2, 1974.

Lacis, A. A. and Hansen, J.: A Parameterization for the Absorption of Solar Radiation in the Earth's Atmosphere., Journal of Atmospheric Sciences, 31, 118–133, https://doi.org/10.1175/1520-0469(1974)031<0118:APFTAO>2.0.CO;2, 1974.

545 Lau, N.-C. and Nath, M. J.: Variability of the Baroclinic and Barotropic Transient Eddy Forcing Associated with Monthly Changes in the Midlatitude Storm Tracks, Journal of Atmospheric Sciences, 48, 2589 – 2613, https://doi.org/10.1175/1520-0469(1991)048<2589:VOTBAB>2.0.CO;2, 1991.

Laursen, L. and Eliasen, E.: On the effects of the damping mechanisms in an atmospheric general circulation model, Tellus Series A, 41, 385–400, https://doi.org/10.3402/tellusa.v41i5.11848, 1989.

550 Levine, R. C. and Turner, A. G.: Dependence of Indian monsoon rainfall on moisture fluxes across the Arabian Sea and the impact of coupled model sea surface temperature biases, Climate Dynamics, 38, 2167–2190, https://doi.org/10.1007/s00382-011-1096-z, 2012.

Li, G. and Xie, S.-P.: Origins of tropical-wide SST biases in CMIP multi-model ensembles, Geophysical Research Letters, 39, https://doi.org/10.1029/2012GL053777, 2012.

Li, G., Xie, S.-P., and Du, Y.: Monsoon-Induced Biases of Climate Models over the Tropical Indian Ocean, Journal of Climate, 28, 3058–
555 3072, https://doi.org/10.1175/JCLI-D-14-00740.1, 2015.

Lindzen, R. S. and Nigam, S.: On the Role of Sea Surface Temperature Gradients in Forcing Low-Level Winds and Convergence in the Tropics, Journal of the Atmospheric Sciences, 44, 2418–2436, https://doi.org/10.1175/1520-0469(1987)044<2418:OTROSS>2.0.CO;2, 1987.

Louis, J.-F.: A parametric model of vertical eddy fluxes in the atmosphere, Boundary-Layer Meteorology, 17, 187–202,
560 https://doi.org/10.1007/BF00117978, 1979.

Louis, J. F., Tiedtke, M., and Geleyn, M.: A short history of the PBL parameterisationv at ECMWF, in: Proceedings, ECMWF workshop on planetary boundary layer parameterization, pp. 59–80, Amer. Meteor. Soc., Reading, 1982.

Lyon, B.: Biases in CMIP5 Sea Surface Temperature and the Annual Cycle of East African Rainfall, Journal of Climate, 33, 8209–8223, https://doi.org/10.1175/JCLI-D-20-0092.1, 2020.

565 Matsuno, T.: Quasi-Geostrophic Motions in the Equatorial Area, Journal of the Meteorological Society of Japan. Ser. II, 44, 25–43, https://doi.org/10.2151/jmsj1965.44.1_25, 1966.

McKenna, S., Santoso, A., Gupta, A. S., Taschetto, A. S., and Cai, W.: Indian Ocean Dipole in CMIP5 and CMIP6: characteristics, biases, and links to ENSO, Scientific Reports, 10, 11 500, https://doi.org/10.1038/s41598-020-68268-9, 2020.

Orszag, S. A.: Transform Method for the Calculation of Vector-Coupled Sums: Application to the Spectral Form of the Vorticity Equation., Journal of Atmospheric Sciences, 27, 890–895, https://doi.org/10.1175/1520-0469(1970)027<0890:TMFTCO>2.0.CO;2, 1970.

Plumb, R. A.: On the Three-Dimensional Propagation of Stationary Waves, Journal of Atmospheric Sciences, 42, 217 – 229, https://doi.org/10.1175/1520-0469(1985)042<0217:OTTDPO>2.0.CO;2, 1985.

Poli, P., Hersbach, H., Dee, D. P., Berrisford, P., Simmons, A. J., Vitart, F., Laloyaux, P., Tan, D. G. H., Peubey, C., Thépaut, J.-N., Trémolet, Y., Hólm, E. V., Bonavita, M., Isaksen, L., and Fisher, M.: ERA-20C: An Atmospheric Reanalysis of the Twentieth Century, Journal of Climate, 29, 4083 – 4097, https://doi.org/10.1175/JCLI-D-15-0556.1, 2016.

Prodhomme, C., Terray, P., Masson, S., Izumo, T., Tozuka, T., and Yamagata, T.: Impacts of Indian Ocean SST biases on the Indian Monsoon: as simulated in a global coupled model, Climate Dynamics, 42, 271–290, https://doi.org/10.1007/s00382-013-1671-6, 2014.

Roeckner, E., Arpe, K., Bengtsson, L., Brinkop, S., Ďumenil, L., Esch, M., Kirk, E., Lunkeit, F., Ponater, M., Rockel, B., Sausen, R., Schlese, U., Schubert, S., and Windelband, M.: Simulation of the present-day climate with the ECHAM-3 model: Impact of model physics and resolution, 1992.

Roxy, M. K., Ritika, K., Terray, P., and Masson, S.: The Curious Case of Indian Ocean Warming, Journal of Climate, 27, 8501–8509, https://doi.org/10.1175/JCLI-D-14-00471.1, 2014.

Sardeshmukh, P. D. and Hoskins, B. J.: The Generation of Global Rotational Flow by Steady Idealized Tropical Divergence, Journal of Atmospheric Sciences, 45, 1228 – 1251, https://doi.org/10.1175/1520-0469(1988)045<1228:TGOGRF>2.0.CO;2, 1988.

Sasamori, T.: The Radiative Cooling Calculation for Application to General Circulation Experiments., Journal of Applied Meteorology, 7, 721–729, https://doi.org/10.1175/1520-0450(1968)007<0721:TRCCFA>2.0.CO;2, 1968.

Schott, F. A., Xie, S.-P., and McCreary, J. P.: Indian Ocean circulation and climate variability, Reviews of Geophysics, 47, RG1002, https://doi.org/10.1029/2007RG000245, 2009.

Slingo, A. and Slingo, J. M.: Response of the National Center for Atmospheric Research community climate model to improvements in the representation of clouds, J. Geoph. Res., 96, 15,341–15,357, https://doi.org/10.1029/91JD00930, 1991.

Stephens, G. L.: Radiation Profiles in Extended Water Clouds. II: Parameterization Schemes., Journal of Atmospheric Sciences, 35, 2123–2132, https://doi.org/10.1175/1520-0469(1978)035<2123:RPIEWC>2.0.CO;2, 1978.

Stephens, G. L.: The Parameterization of Radiation for Numerical Weather Prediction and Climate Models, Monthly Weather Review, 112, 826, https://doi.org/10.1175/1520-0493(1984)112<0826:TPORFN>2.0.CO;2, 1984.

Trenberth, K. E., Branstator, G. W., Karoly, D., Kumar, A., Lau, N.-C., and Ropelewski, C.: Progress during TOGA in understanding and modeling global teleconnections associated with tropical sea surface temperatures, Journal of Geophysical Research: Oceans, 103, 14 291–14 324, https://doi.org/https://doi.org/10.1029/97JC01444, 1998.

Turner, A. G., Inness, P. M., and Slingo, J. M.: The role of the basic state in the ENSO-monsoon relationship and implications for predictability, Quarterly Journal of the Royal Meteorological Society, 131, 781–804, https://doi.org/10.1256/qj.04.70, 2005.

Vecchi, G. A. and Harrison, D. E.: Monsoon Breaks and Subseasonal Sea Surface Temperature Variability in the Bay of Bengal, Journal of Climate, 15, 1485–1493, https://doi.org/10.1175/1520-0442(2002)015<1485:MBASSS>2.0.CO;2, 2002.

Žagar, N., Kasahara, A., Terasaki, K., Tribbia, J., and Tanaka, H.: Normal-mode function representation of global 3-D data sets: open-access software for the atmospheric research community, Geoscientific Model Development, 8, 1169–1195, https://doi.org/10.5194/gmd-8-1169-2015, 2015.

Žagar, N., Kosovelj, K., Manzini, E., Horvat, M., and Castanheira, J.: An assessment of scale-dependent variability and bias in global prediction models, Climate Dynamics, 54, 287–306, https://doi.org/10.1007/s00382-019-05001-x, 2020.

Wang, C., Zhang, L., Lee, S.-K., Wu, L., and Mechoso, C. R.: A global perspective on CMIP5 climate model biases, Nature Climate Change, 4, 201–205, https://doi.org/10.1038/nclimate2118, 2014.

Wang, Y., Heywood, K. J., Stevens, D. P., and Damerell, G. M.: Seasonal extrema of sea surface temperature in CMIP6 models, Ocean Science, 18, 839–855, https://doi.org/10.5194/os-18-839-2022, 2022.

Weller, E. and Cai, W.: Asymmetry in the IOD and ENSO Teleconnection in a CMIP5 Model Ensemble and Its Relevance to Regional Rainfall, Journal of Climate, 26, 5139–5149, https://doi.org/10.1175/JCLI-D-12-00789.1, 2013.

Wettstein, J. J. and Wallace, J. M.: Observed Patterns of Month-to-Month Storm-Track Variability and Their Relationship to the Background Flow, Journal of the Atmospheric Sciences, 67, 1420 – 1437, https://doi.org/10.1175/2009JAS3194.1, 2010.

Zhang, Q., Liu, B., Li, S., and Zhou, T.: Understanding Models' Global Sea Surface Temperature Bias in Mean State: From CMIP5 to CMIP6, Geophysical Research Letters, 50, e2022GL100 888, https://doi.org/https://doi.org/10.1029/2022GL100888, 2023.

Zhang, Y. and Liang, X. S.: The distinct PNA pattern induced by the South China Sea, Climate Dynamics, https://doi.org/10.1007/s00382-022-06607-4, 2022.

Zhao, Y.-B. and Liang, X. S.: On the Inverse Relationship between the Boreal Wintertime Pacific Jet Strength and Storm-Track Intensity, Journal of Climate, 31, 9545 – 9564, https://doi.org/10.1175/JCLI-D-18-0043.1, 2018.